



Ontario Winter Lake-effect Systems (OWLeS): Bulk Characteristics and Kinematic Evolution of Misovortices in Long-Lake-Axis-Parallel Snowbands

KAREN A. KOSIBA AND JOSHUA WURMAN

Center for Severe Weather Research, Boulder, Colorado

KEVIN KNUPP AND KYLE PENNINGTON

University of Alabama at Huntsville, Huntsville, Alabama

PAUL ROBINSON

Center for Severe Weather Research, Boulder, Colorado

(Manuscript received 13 June 2019, in final form 30 September 2019)

ABSTRACT

During the Ontario Winter Lake-effect Systems (OWLeS) field campaign, 12 long-lake-axis-parallel (LLAP) snowband events were sampled. Misovortices occurred in 11 of these events, with characteristic diameters of ~ 800 m, differential velocities of ~ 11 m s⁻¹, and spacing between vortices of ~ 3 km. A detailed observational analysis of one such snowband provided further insight on the processes governing misovortex genesis and evolution, adding to the growing body of knowledge of these intense snowband features. On 15–16 December 2013, a misovortex-producing snowband was exceptionally well sampled by ground-based OWLeS instrumentation, which allowed for integrated finescale dual-Doppler and surface thermodynamic analyses. Similar to other studies, horizontal shearing instability (HSI), coupled with stretching, was shown to be the primary genesis mechanism. The HSI location was influenced by snowband-generated boundaries and location of the Arctic front relative to the band. Surface temperature observations, available for the first time, indicated that the misovortices formed along a baroclinic zone. Enhanced mixing, higher radar reflectivity, and increased precipitation rate accompanied the vortices. As the snowband came ashore, OWLeS participants indicated an increase in snowfall and white out conditions with the passage of the snowband. A sharp, small-scale pressure drop, coupled with winds of ~ 16 m s⁻¹, marked the passage of a misovortex and may be typical of snowband misovortices.

1. Introduction

Some of the world's most intense lake-effect snow events occur downstream of the North American Great Lakes. Lake-effect snow events often only impact a relatively small area, but, within that narrow corridor,

snowfall amounts and rates can be substantial. Lake-effect snowbands are relatively shallow, ~ 2 – 3 km deep, and, consequently, Weather Surveillance Radar-1988 Doppler (WRS-88D) coverage of these events from long ranges can be insufficient to capture many of the small-scale structures that are considered important for snow production and/or local variations in snowfall rates (e.g., [Winstead et al. 2001](#)). Snowbands that form parallel to the long axis of the lakes, long-lake-axis-parallel (LLAP) (e.g., [Steiger et al. 2013](#)), or Type 1 bands (e.g., [Niziol et al. 1995](#)) most frequently occur along Lakes Ontario and Erie due to the orientation of the prevailing environmental winds along the major axis of these lakes ([Kristovich and Steve 1995](#); [Rodriguez et al. 2007](#); [Laird et al. 2017](#)). These bands have a large major-to-minor

Denotes content that is immediately available upon publication as open access.

Supplemental information related to this paper is available at the Journals Online website: <https://doi.org/10.1175/MWR-D-19-0182.s1>.

Corresponding author: Karen A. Kosiba, kakosiba@cswr.org

DOI: 10.1175/MWR-D-19-0182.1

© 2019 American Meteorological Society. For information regarding reuse of this content and general copyright information, consult the [AMS Copyright Policy](#) (www.ametsoc.org/PUBSReuseLicenses).

axis ratio (i.e., they are long and narrow), can be the most convectively active (e.g., Moore and Orville 1990; Niziol et al. 1995; Steiger et al. 2018), and frequently are associated with intense localized snowfall along and near the downwind shoreline. For example, just east of Buffalo, New York, a LLAP event produced ~ 165 cm of lake-effect snow accumulation over a 48-h period, from 17 to 19 November 2014, closing roads, causing structural failures, and contributing to several fatalities. Since these snowbands are so narrow, the gradient in snowfall can be quite sharp, such as in the 17–19 November 2014 storm where regions just a few kilometers from the snow maximum only had snow totals of ~ 15 cm (National Weather Service 2014). Heterogeneities within snowbands, such as mesoscale and misoscale vortices, can locally impact snowfall rates and wind speeds, but the type, frequency of occurrence, kinematics, genesis mechanisms, and impacts are still active areas of research.

Mesoscale vortices, typically defined as vortices with diameters of ~ 4 – 100 km, have been documented in snow events over, predominantly, the western Great Lakes (e.g., Forbes and Merritt 1984; Pease et al. 1988; Laird 1999; Laird et al. 2001; Grim et al. 2004), but not until recently have misoscale vortices, those with diameters ≤ 4 km, been investigated over the eastern Great Lakes (Steiger et al. 2013). Using finescale single-Doppler mobile radar observations from two LLAP events, Steiger et al. (2013) first documented misovortex characteristics within a small sampling of LLAP bands over Lake Ontario. Typically, the vortices had diameters (D), defined as the distance between maximum inbound and outbound Doppler velocities, of ≤ 1 km and differential velocities (ΔV), defined as the difference between maximum inbound and outbound observed Doppler velocities, of ≤ 11 m s^{-1} . Steiger et al. (2013) hypothesized that the structures occurred as a result of horizontal shear instability (HSI) and may impact the precipitation type and/or rate. But, since only single-Doppler radar observations were available, this precluded a detailed kinematic analysis of these features. Circulations with $D \geq 1.5$ km also were documented, but these structures were comparatively rare.

More recently, using numerical model and dual-Doppler analyses of a LLAP event observed during the Ontario Winter Lake-effect Systems (OWLeS) project (Kristovich et al. 2017), Mulholland et al. (2017) [M17 hereafter] investigated the role of HSI in misovortex formation during the seventh Intensive Operations Period (IOP7 hereafter). In both the observational and model analyses, they found that shearing instability criteria were satisfied when misovortices were present, supporting HSI as the genesis mechanism. The vortices were observed to

weaken at landfall, and it was inferred from modeling results that the combination of increased surface roughness and reduced stretching due to the decrease in low-level updraft strength as warming from the lake surface ended contributed to the demise of the misovortices.

Misovortices also have been observed downwind of the Sea of Japan during cold air outbreaks (e.g., Inoue et al. 2011; Inoue et al. 2016). Inoue et al. (2011) documented the occurrence of four misovortices within the comma echo of a winter system, one of which was associated with F0 damage. The misovortices dissipated quickly after landfall, which the authors attributed to, in part, an increase surface friction. The genesis mechanism was unclear, but the misovortices formed along a convergence line and subsequent stretching of vertical vorticity by convection overhead was the assumed mechanism. During another event, at least five misovortices were documented along a convergence line, which also suggested that HSI had a role in genesis (Inoue et al. 2016). Observations from two surface weather stations of one of the vortices recorded wind speeds of ~ 20 – 25 m s^{-1} and pressure drops of ~ 0.6 – 1 mb. In contrast to Inoue et al. (2011) and M17, as one of the vortices made landfall, the tangential velocities were observed to increase, which was attributed to an increase in stretching as a result of increased convergence and a decrease in vortex radius. Since many of these vortices are observed over open water, the behavior of the vortex line as it interacts with a change in underlying surface and the internal thermodynamics of the snowbands remain relatively unknown.

Misovortex lines are not unique to “cold season” events and have been documented in association with “warm season” convergence boundaries, such as gust fronts, cold fronts, sea breezes, and drylines (e.g., Kingsmill 1995; Friedrich et al. 2005; Pietrycha and Rasmussen 2004; Arnott et al. 2006; Marquis et al. 2007; Buban et al. 2007; Friedrich et al. 2008a,b). They have been hypothesized to be a mechanism for convective initiation (CI) (e.g., Arnott et al. 2006; Marquis et al. 2007) and for the genesis of nonsupercell tornadoes (NST) (e.g., Wakimoto and Wilson 1989). While some investigators cite the interaction of horizontal convective rolls with the convergence boundary as the instigator, others attribute misovortex formation to HSI. Numerical simulations by Lee and Wilhelmson (1997) further investigated the genesis and life cycle of misovortices along an idealized outflow boundary and concluded that HSI is the primary mechanism, with possible contributions from lobe and cleft instability to the initial perturbations along the boundary. Additionally, the misovortices influenced the vertical velocity along the outflow leading edge, with the updrafts playing a critical

role in CI. Whether or not lake-effect snowband misovortices lead to convection enhancement remains unknown.

The field component of OWLeS took place from 5 December 2013 to 29 January 2014 and provided the unique opportunity to examine the finescale four-dimensional structure of misovortex-containing LLAP bands using targeted observations from mobile Doppler radars and other surface assets. M17's dual-Doppler analysis of IOP7 is the first and only such analysis of snowband misovortices, but lacked thermodynamic observations. Moreover, as noted by Steiger et al. (2013) the band-relative location of the misovortices, and hence their genesis mechanism, evolution, and impacts on precipitation production, may vary from case to case. A misovortex-producing snowband that occurred overnight on 15 to 16 December 2013 (IOP4 hereafter) provided an excellent case for observational analysis and comparison to the kinematics first documented in IOP7 by M17. In addition to the benefit of analyzing different cases to understand the generalizability of the results, unlike IOP7, IOP4 had better low-level dual-Doppler coverage, finer spatial resolution, and surface meteorological observations as the LLAP band comes ashore. Last, the sampling of 12 LLAP bands at the same geographical location, by the same instruments, afforded the first opportunity to provide a general context of misovortex characteristics for the interpretation of the findings presented from individual case studies.

The objectives of this research are twofold: 1) examine the kinematic evolution of a *different* snowband than documented in M17 through a detailed multi-instrument case study analysis and 2) compile misovortex characteristics for all misovortex-producing snowbands and compare these bulk characteristics to those reported in case studies. The manuscript is organized as follows. Section 2 provides an overview of the data used in the subsequent analyses. Section 3 focuses on a case study of IOP4, which had some of the best overall dual-Doppler coverage of any misovortex-containing band sampled during OWLeS. The finescale dual-Doppler analyses of a misovortex-containing snowband, coupled with onshore surface weather stations, allowed for investigation of the mechanisms of misovortex genesis and maintenance, kinematic characteristics, effects on microphysics, and contributions to boundary layer momentum fluxes. To put the observations from IOP4 and IOP7 in context with other LLAP snowbands, the misovortex characteristics of all the LLAP snowbands sampled during OWLeS are examined in section 4. Section 5 discusses the relevance of the results.

2. Data

a. Mobile radar data

The Center for Severe Weather Research (CSWR) deployed three Doppler on Wheels (DOW) mobile radars (Wurman 2001) during the OWLeS field campaign. One to three DOWs were deployed for each IOP, but due to split research objectives, DOWs 6 and 7 often were more favorably placed relative to the LLAP snowbands and, consequently, employed a predominantly volumetric surveillance scan strategy from which dual-Doppler analyses could be conducted. Therefore, only data from these radars were used in the dual-Doppler and multicas e misovortex analyses. DOWs 6 and 7 are dual-polarization, dual-frequency radars and operated in “fast-45” mode, both frequencies simultaneously transmit/receive H and V, during OWLeS (CSWR 2019). The DOWs used a $0.4\ \mu\text{s}$ pulse, with matched gate length of 60 m, and had a range of 58 km. A staggered PRF of 2000/2500 Hz increased the Nyquist velocity to $79\ \text{m s}^{-1}$, so manual de-aliasing of the velocity data was unnecessary. Beams were indexed at 0.5° intervals. The 10-min synced DOW scan strategy comprised horizontal surveillance scans, range–height indicator (RHI) scans, and zenith-pointing calibration scans. Time-synced data suitable for volumetric dual-Doppler analysis, comprising elevation angles $0.5^\circ, 1^\circ, 2^\circ, 3^\circ, 4^\circ, 5^\circ, 6^\circ, 7^\circ, 8^\circ, 9^\circ, 10^\circ, 12^\circ, 14^\circ,$ and 16° , occurred every 3–4 min and RHIs, which gave a quasi-instantaneous view of the vertical structure, occurred every 10 min. Zenith scans during light snow were used to determine any drifts in the differential reflectivity (ZDR) during IOPs (e.g., Bringi and Chandrasekar 2001). The DOWs were calibrated prior to the beginning and after the field phase of the project.

b. Dual-Doppler methodology

For IOP4, the DOW6 and DOW7 deployment locations along the southeastern shore of Lake Ontario resulted in a baseline of 17.3 km with a dual-Doppler lobe over the lake (Figs. 1, 4, and 5). Data were objectively analyzed to a Cartesian grid using a two-pass Barnes filter (Majcen et al. 2008) with kappa values of 0.129 in the horizontal ($\kappa_x = \kappa_y$) and 0.518 in the vertical (κ_z) and a second-pass convergence parameter (γ) of 0.3. Grid spacing values of $\Delta x = \Delta y = 100\ \text{m}$ in the horizontal and $\Delta z = 200\ \text{m}$ in the vertical were chosen based on the half-power beamwidth at a distance of $\sim 25\ \text{km}$ from the radars. There was no downward extrapolation in the objective analysis. Dual-Doppler analyses were conducted using the CSWR version of the OPAWS software, which extrapolates the

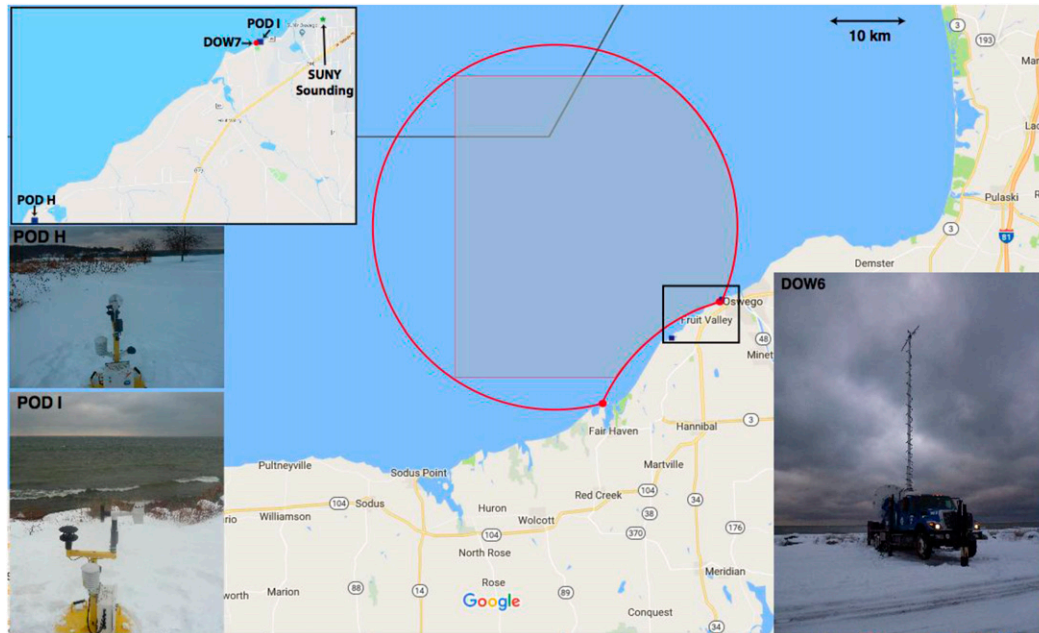


FIG. 1. Overview of the deployment of OWLeS assets used in the IOP4 analysis. Inset shows a zoomed-in view of the area enclosed by the black rectangle. Red dots indicate the DOW6 and DOW7 locations. Blue squares indicate the Pod locations. The DOW6–DOW7 dual-Doppler lobe is shown in red, with the shaded area depicting the standard dual-Doppler domain. No picture of DOW7 was available for this IOP.

geometric coefficients downward and solves iteratively for u , v , and w (see appendix A of Kosiba et al. 2013 for more details). The dual-Doppler domain comprised a volume of $X = Y = 40$ km and $Z = 3.5$ km. Translation corrections were applied to account for band propagation between the scans and the nominal dual-Doppler analysis times. Later in the analysis period, from 0550 to 0600 UTC, the band and misovortices were much closer to both radars (Fig. 5d), so, in addition to the standard grids described above, smaller-sized grids ($X = 30$ km; $Y = 8$ km; $Z = 3.5$ km), with finer spatial resolution ($\Delta x = \Delta y = 50$ m; $\Delta z = 100$ m) ($\kappa_x = \kappa_y = 0.03$; $\kappa_z = 0.12$) were created to better resolve smaller spatial scale details. Both the “standard” and “small” grids resolved structures with characteristic smallest wavelengths of 300 to 600 m (e.g., Trapp and Doswell 2000) and were the finest dual-Doppler grids, to date, used to look at misovortex structure in lake effect snowbands. Qualitatively, both the “standard” and “small” grids depict the same structures. During the early part of the analysis period, from 0520 to 0540 UTC, the dual-Doppler coverage of the entire snowband is quite good, whereas after 0550 UTC, beam blockage southwest of DOW 7 precluded dual-Doppler coverage of the southern periphery of the band (Fig. 5d). But, at this time, the vortices were located in the north–north-central (trailing) portion of the southward propagating snowband, which was well within the dual-Doppler

domain. So, the area containing these vortices was still able to be analyzed.

c. Additional observations

In addition to data from the DOWs, data from ground-based instruments were integrated into the IOP4 analysis (Fig. 1). CSWR deployed a network of 10 weather stations (Pods) that measured 1 Hz temperature, wind speed/direction, and pressure 1-m above ground level (AGL) (CSWR 2019). During IOP4, two Pods, Pod I and Pod H, were optimally located near the shoreline to sample the thermodynamic and surface wind characteristics associated with the snowband. Proximal ~ 3 -h soundings¹, launched from/by the State University of New York (SUNY) Oswego, were used to characterize the local environment in tandem with dual-polarization fields for hydrometeor identification within the band. The sounding launches were all south of the band during the analysis period.

The DOWs were equipped with 18-m AGL masts that sampled temperature, relative humidity, wind speed, and wind direction at 1 Hz frequency. But, for IOP4, the DOW7 mast was not raised, so all mast measurements were taken at ~ 4 m AGL. The temperature and relative humidity data are suspect, and not presented, since they

¹ Vaisala RS92-SGP sondes.

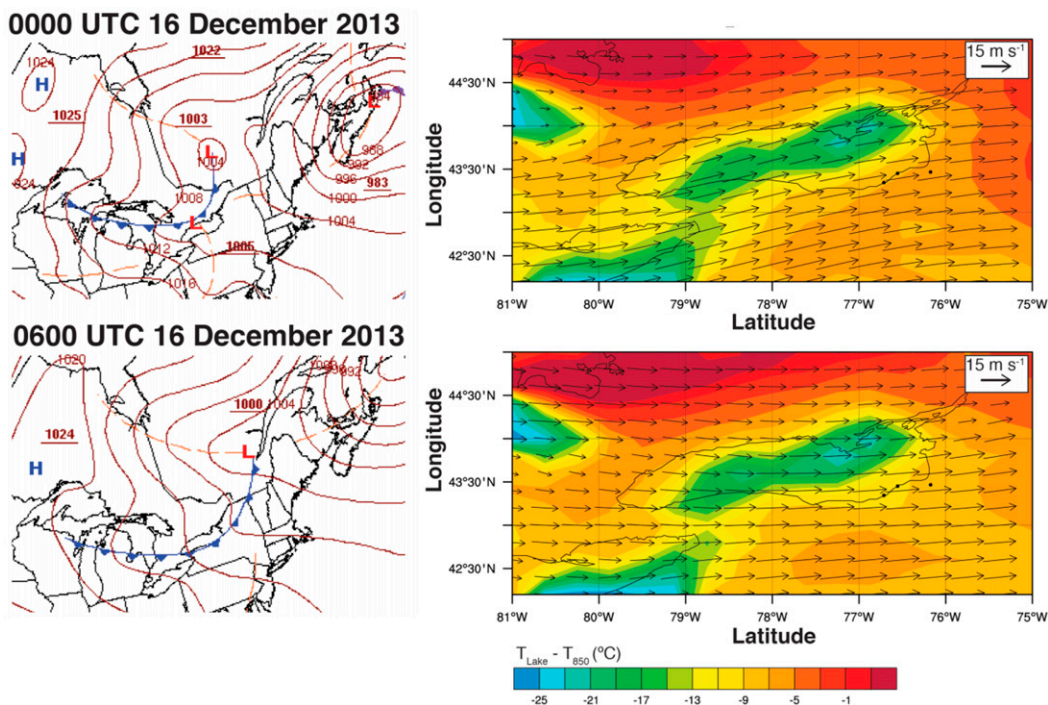


FIG. 2. Overview of the large-scale environment during IOP4. (top) (left) Surface analysis from the Weather Prediction Center and (right) difference between the surface temperature of Lake Ontario and the 850 mb temperature at 0000 UTC 16 Dec 2013. (bottom) (left) Surface analysis from the Weather Prediction Center and (right) difference between the surface temperature of Lake Ontario and the 850 mb temperature at 0600 UTC 16 Dec 2013. (top and bottom right panels) Vector winds at 850 mb are overlaid on the temperature difference plots at the respective times. The Arctic front was located north of Lake Ontario at 0000 UTC 16 Dec 2013 and, by 0600 UTC 16 Dec 2013, the front was near the southern shore of Lake Ontario. The 850 mb winds become more northerly by 0600 UTC 16 Dec 2013.

likely were contaminated by generator exhaust. The overall trends in the wind speed and direction likely were reliable and have been confirmed with observations from a nearly collocated Pod, but small fluctuations occurred due to proximity to the rotating antenna. The pressure sensor was located inside the radar cab at approximately the same height as the lowered mast and was not impacted by the generator or rotating antenna.

3. Case study of a misovortex-producing snowband: IOP4

a. Overview of the case

IOP4 occurred overnight from 15 to 16 December 2013 and was associated with the passage of an Arctic front that approached the OWLeS domain from the north (Fig. 2). Ahead of the front, westerly winds developed across Lake Ontario. Reanalysis data from the National Centers for Environmental Prediction (NCEP) at 0000 and 0600 UTC 16 December 2013 indicated the difference between the lake surface and the

850 mb temperatures ($T_{\text{lake}} - T_{850}$) ranged from -10° to -22°C (Fig. 2), within the 13°C threshold commonly used for boundary layer instability (Holroyd 1971). Proximal sounding data from SUNY Oswego at 0215 and at 0459 UTC 16 December showed a nearly unidirectional, primarily westerly, wind profile throughout the boundary layer. The 0–1 km shear values were 17 m s^{-1} at 0215 UTC and 14 m s^{-1} at 0459 UTC; the 0–3 km shear values were 24 and 13 m s^{-1} at 0215 and 0459 UTC, respectively (Fig. 3). Using the equilibrium height as a predictor of band intensity (e.g., Byrd et al. 1991), sounding data indicated that this occurred at $\sim 3\text{ km}$, sufficient for a LLAP event (Fig. 3). The cold air, coupled with strong low-level westerly flow and sufficient instability was conducive to the formation and maintenance of a LLAP snowband that would impact the east and southeast shores of Lake Ontario (e.g., Niziol 1987).

The DOWs observed the evolution of the LLAP snowband from approximately 2100 UTC 15 December to 0630 UTC 16 December 2013 (see the animation in the online supplemental material). The band underwent

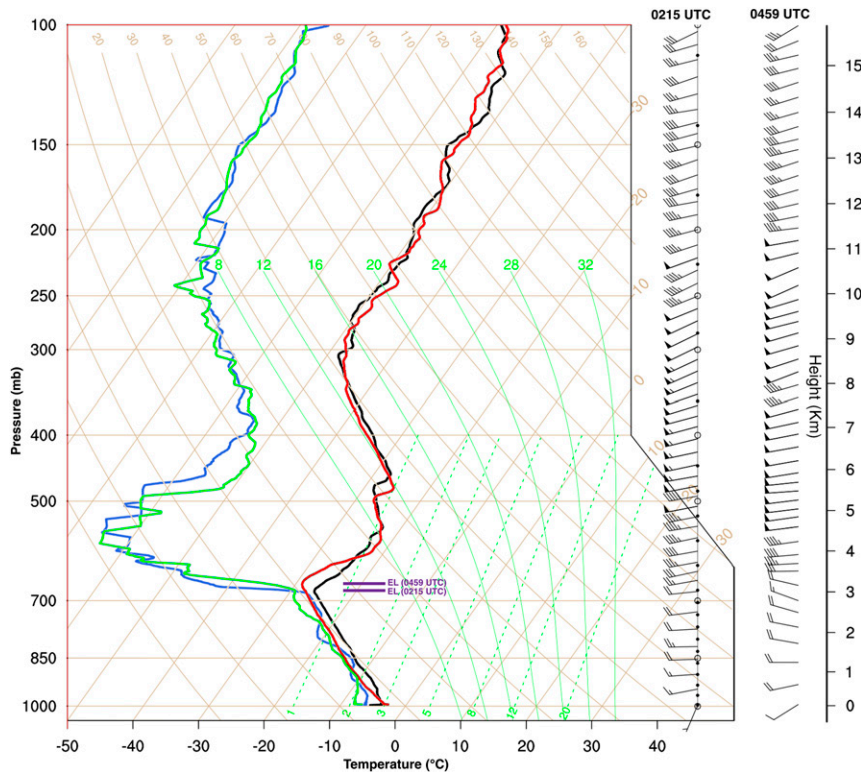


FIG. 3. Skew T -log p plots of the vertical profiles of temperature, dewpoint temperature, and winds obtained from the soundings launched at the SUNY Oswego campus at 0215 UTC 16 Dec and at 0459 UTC 16 Dec 2013. The black line depicts the temperature profile and the blue line depicts the dewpoint temperature profile from the 0215 UTC 16 Dec 2013 sounding. The red line depicts the temperature profile and the green line depicts the dewpoint temperature profile from the 0459 UTC 16 Dec 2013 sounding. Wind barbs are shown in m s^{-1} . Pressure, in mb, is shown on the left vertical axis; height, in km, is shown on the far right vertical axis. Both soundings have an equilibrium level, indicated by the purple horizontal lines, of ~ 3 km and a mostly unidirectional, westerly, wind profile throughout the depth of the sounding.

significant structural evolution during the ~ 9.5 -h IOP (Figs. 4 and 5). The snowband initially formed under west-northwesterly flow and became more organized around 2300 UTC with the major axis oriented approximately east-west across eastern Lake Ontario. From ~ 2330 to ~ 0200 UTC, the snowband was relatively narrow (~ 20 km, defined by the minor axis of reflectivity) and there was a line of weak misovortices located near the southern edge of the band (Figs. 4a,b). A prominent misovortex line occurred between 0110 and 0140 UTC as the snowband moved southward (Fig. 4b). After 0200 UTC, the band became less defined and had a broad region of precipitation, with occasional transient vortices and higher reflectivity cells (Fig. 4c). By 0340 UTC, the precipitation reorganized, initially as a diffuse double-banded structure, with a line of weak vortices near the southern edge of the northern snowband (Fig. 4d). It was likely that the northern snowband was associated with the Arctic front because the winds north of the vortex line

had increased from earlier and, soon after that time (~ 0420 UTC), the precipitation had a continuous southward movement at $\sim 3 \text{ m s}^{-1}$, similar to the analyzed position and movement of the Arctic front. The wind speed perturbations associated with the misovortices were generally $4\text{--}9 \text{ m s}^{-1}$ above the background flow.

By 0430 UTC, the northern region of precipitation had mostly merged with the southern region (Fig. 5a) and, by 0504 UTC, a dominant, narrow (minor axis of reflectivity ~ 10 km) snowband emerged, with a line of misovortices transecting the band from southeast to northwest; the southeastern vortices were near the southern edge of the band and the northwestern vortices were near the northern edge of the band (Fig. 5b). By 0530 UTC, the maximum reflectivity associated with the band also had increased from prior values of 20–25 dBZ to values of 30–35 dBZ (Fig. 5c). The misovortices generally had a $\sim 15\text{--}16 \text{ m s}^{-1}$ eastward propagation speed, parallel to the long axis of the snowband, along a

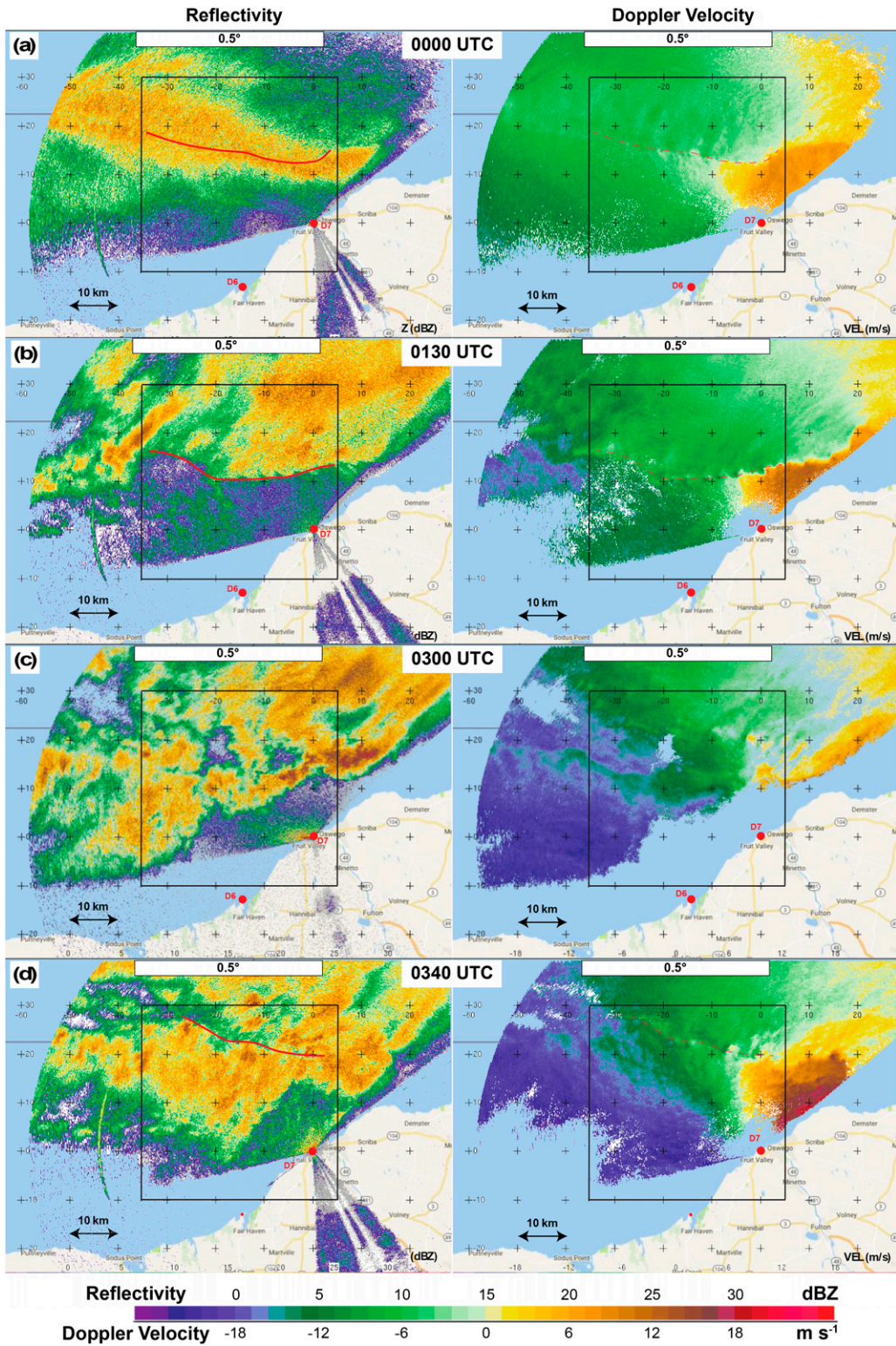


FIG. 4. Evolution of the LLAP band at select times discussed in the text during IOP4. (left) DOW7 radar reflectivity and (right) DOW7 Doppler velocity; both are shown at 0.5° elevation. The red dots indicate the DOW6 (D6) and DOW7 (D7) locations. When present, the vortex line is annotated by a thin dashed line in the Doppler velocity field and a solid red line in the reflectivity field.

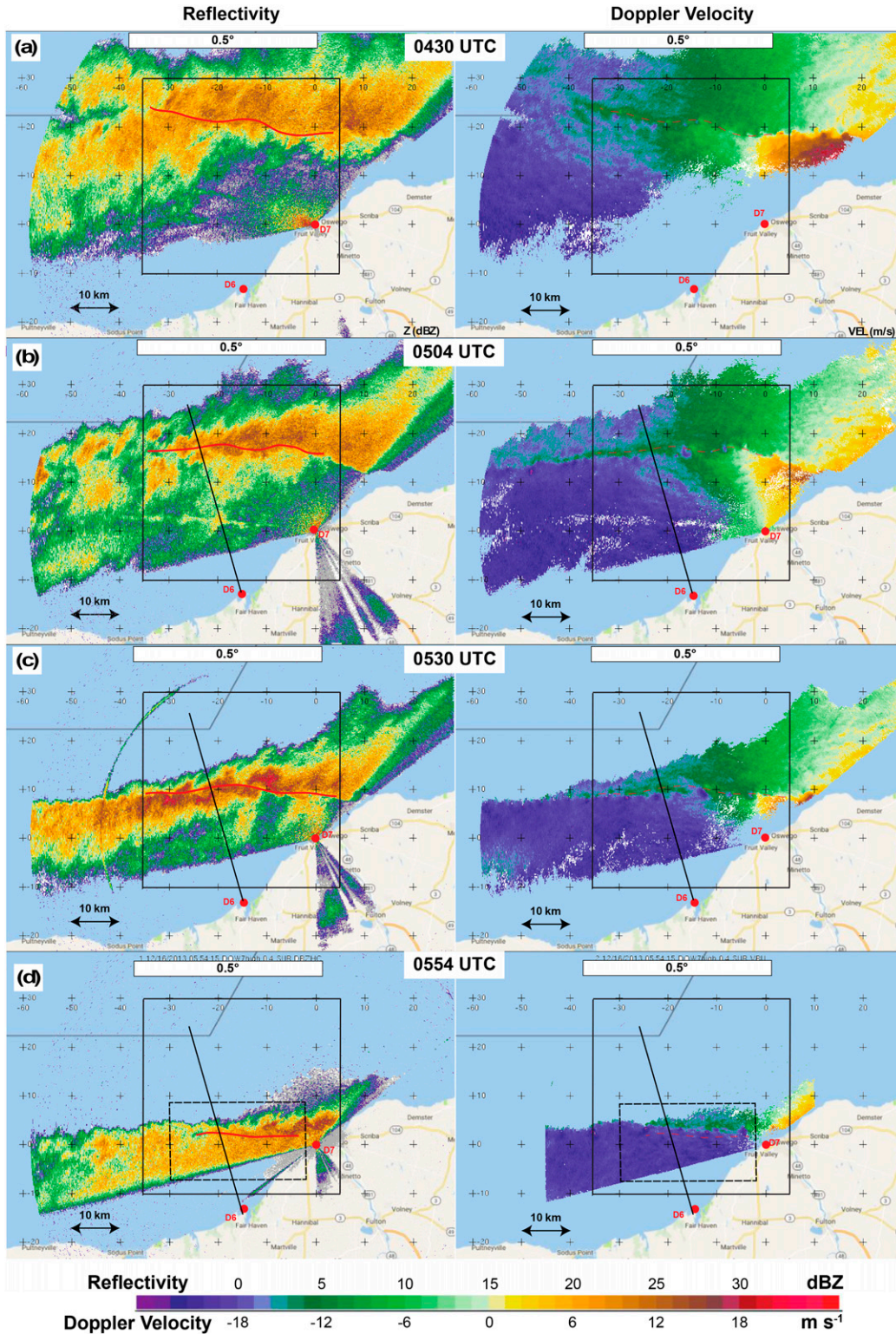


FIG. 5. Evolution of the LLAP band at select times discussed in the text during IOP4. (left) DOW7 radar reflectivity and (right) DOW7 Doppler velocity; both are shown at 0.5° elevation. The red dots indicate the DOW6 (D6) and DOW7 (D7) locations. The black lines in (b)–(d) depict the location of the RHIs shown in Fig. 6. When present, the vortex line is annotated by a thin dashed line in the Doppler velocity field and a solid red line in the reflectivity field.

region of inferred convergence, similar to the misovortex and dust devil observations of Pietrycha and Rasmussen (2004). The band structure, with associated misovortices, and southward movement, remained relatively persistent until the end of the observation period when the LLAP band moved in close proximity to DOW7 (Fig. 5d).

Evolution of the vertical structure of the misovortex-bearing convergence zone was inferred from RHIs (Fig. 6). The RHIs from DOW6 at 344° azimuth had the best observing geometry, which was approximately perpendicular to the long axis of the snowband (Figs. 5b–d). Initially, between 0503 and 0533 UTC (Figs. 6a,b), near the southern edge of precipitation, there was a pronounced backward/northern tilt of the convergence region with height. But, from 0533 UTC onward, the convergence region had migrated to near the northern end of the high reflectivity region and it had a more upright vertical structure than earlier (Figs. 6c–e). The initial backward slope with height might be indicative of cooler/less buoyant air undercutting relatively warmer/more buoyant air ahead of the line, suggesting distinctly different air masses on either side of the misovortex line, such as observed by Bergmaier et al. (2017). Indeed, surface observations, discussed in subsequent sections, suggest the presence of thermodynamic boundaries.

The DOW7 mesonet and the approximately collocated Pod I data showed an increase in wind speed and variability (“gustiness”) after ~0230 UTC, which is associated with a change in wind direction as the front/band had moved south of the DOW7/Pod I location (Figs. 7a,b). Pressure generally was increasing during this period (Fig. 7c) and temperature was generally decreasing from ~0300 UTC onward (Fig. 7d). These overall trends likely were associated with the arrival/stalling of the Arctic front near the southeastern shore of Lake Ontario. The observed small-scale decrease in pressure at ~0605 UTC was shown to be associated with the passage of a misovortex and the small-scale warming between ~0600 and ~0620 UTC was associated with the passage of the band.

After ~0620 UTC, the eastern extent of the band/front was inland, south of the DOW7 and Pod I location. Data from Pod H, which had a more southerly location, recorded the passage of a misovortex ~0628 UTC, as indicated by similar pressure and wind trends as observed earlier in the DOW7 mesonet and Pod I data. Pod H also experienced a brief warming between ~0628 and ~0637 UTC and both Pod I and Pod H recorded decreasing temperatures after the snowband moved over their locations.

Misovortices were present for long periods, but not continuously, throughout the IOP. Occasionally,

anticyclonic misovortices (Fig. 8c) and mesoscale vortices were present (Fig. 8b). Additionally, early in the IOP, in the single-Doppler velocity data, there was evidence of linear streaks, manifested as alternating regions of maximum and minimum Doppler velocities (Fig. 8a), which can be characteristic of sheared boundary layers (e.g., Khanna and Brasseur 1998; Foster 2005). But, unlike warm season radar observations, there was very little radar return outside of the precipitation, so three-dimensional boundary layer observations of the environment immediately outside of the band were limited. The prolonged occurrence of misovortices, coupled with favorable dual-Doppler geometry and near-shore surface station observations, allowed for an in-depth analysis of LLAP band kinematics and a further understanding of misovortex processes and their potential impacts.

The focus of this research is on the evolution of the snowband late in the IOP, from 0520 to 0600 UTC, when the snowband is in close proximity to the DOWs, affording high-resolution analyses of subband-scale features. During this period, a prominent line of the strongest and greatest number of IOP-observed vortices occurred and the surface meteorological observations from the coastally located Pods (“I” and, to a lesser extent, “H”) and DOW7 can be linked to snowband characteristics and internal processes.

b. LLAP band kinematic structure

The dual-Doppler analyses revealed regions of coherent vertical vorticity (ζ) embedded in the snowband throughout the 0500–0600 UTC period (Figs. 8 and 9). The median spacing between vortices ranged from ~2.5 to 4.0 km, and the spacing varied from volume to volume. The most intense vortices occurred between 0530 and 0600 UTC. Using 0.01 s^{-1} as the lower bound on ζ , typically 5–8 misovortices were present in each dual-Doppler volume. Vertical vorticity values typically were on the order of 0.02 s^{-1} , but in the stronger vortices approached 0.04 s^{-1} (Fig. 9). Exact magnitudes of ζ , of course, are impacted by the smoothing parameters used in the objective analyses and misovortices with ζ values of 0.08 s^{-1} were analyzed in the small grid retrievals (Fig. 10). For comparison, during this period, single-Doppler calculations of implied ζ , using $2 \times (\Delta V/D)$, ranged from 0.011 to 0.201 s^{-1} , with a median value of 0.026 s^{-1} .

The lifetime of individual vortices was variable, with some of the most persistent vortices lasting upward of 50 min. As an example, three misovortices were tracked during part of the dual-Doppler analysis period. Figures 9 and 10 show the locations of these three vortices, A, B, and C, at each analysis time. The individual

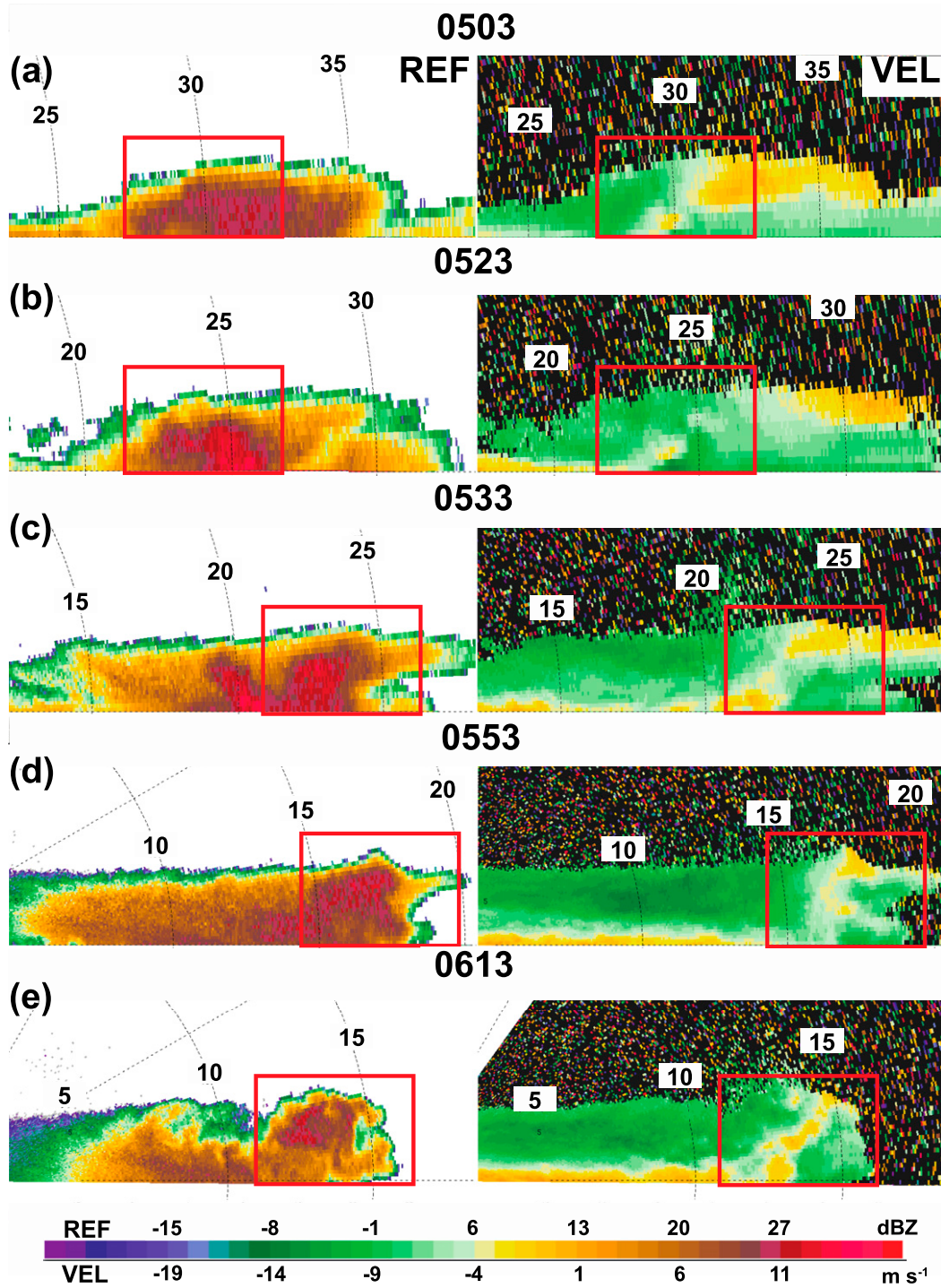


FIG. 6. RHIs from DOW6 during the analysis period, from 0503 to 0613 UTC. RHIs all are at 344° azimuth, as shown in Figs. 5b–d, and are approximately band-perpendicular. (left) Radar reflectivity and (right) Doppler velocity. The Doppler velocity color table has been adjusted to account for band motion. Range rings, from DOW6, are shown at 5 km intervals. The red rectangle depicts the misovortex-bearing convergence region.

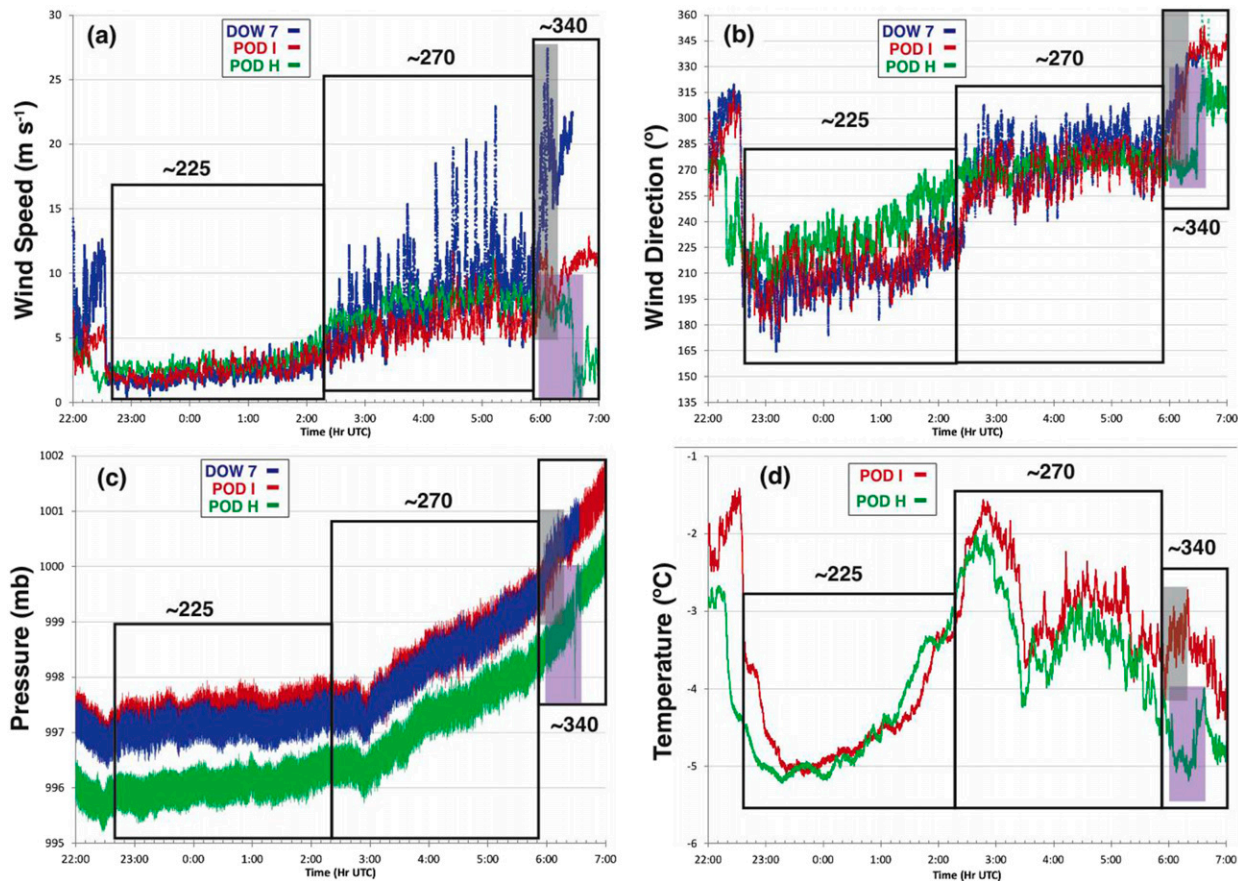


FIG. 7. Observations from the DOW7 (blue), Pod I (red), and Pod H (green) weather stations from 2300 UTC 15 Dec to 0700 UTC 16 Dec. Depicted are: (a) the 1-min averaged wind speed in m s^{-1} , (b) the 1-min averaged wind direction in degrees, (c) the 3-s averaged pressure in mb, and (d) the 1-min averaged temperature in $^{\circ}\text{C}$. The different wind direction regimes are denoted by the black rectangles, with the approximate wind direction regime labeled accordingly, and the snowband passage is denoted by the gray shading over Pod I and DOW7 and by the purple shading over Pod H. The snowband first passes over DOW7 and Pod I and then over Pod H. Although DOW7 wind measurements were impacted by the movement of the antenna, they were shown to corroborate the general trends shown in the Pod observations.

vortices remained identifiable in time and were in the dual-Doppler domain for ~ 30 min, consistent with a $\sim 15 \text{ m s}^{-1}$ eastward propagation speed across the band. Vertical cross sections through these three misovortices at select times between 0520 and 0554 UTC offered additional insight on their structures and local environment within the snowband (Figs. 11 and 12). The misovortices generally were located in or near a region of upward motion (Figs. 9–11). The vortices were strongest near the surface, coherent with height, and extended through the depth of the domain (Fig. 12). Evaluation of the along-band horizontal wind shear, defined by du/dy , where u is the horizontal velocity in the x , or east–west, direction and y is the north–south horizontal distance perpendicular to u , revealed that the vortices formed in a narrow region of maximum du/dy , which was strongest near the surface. Both ζ and du/dy were similarly sloped with height,

suggesting the importance of du/dy in the generation of ζ , and hence misovortex formation. Stretching of ζ (hereafter “stretching”) also was maximum near the surface and coincident with ζ , providing a mechanism for misovortex maintenance (Fig. 12).

Similar to other studies of misovortex lines (e.g., Lee and Wilhelmson 1997), kinks in the vertical velocity (Figs. 9 and 10) and along-band horizontal wind shear (not shown) developed coincident with the vortices. It has been suggested (e.g., Steiger et al. 2013; M17) that this type of misovortex configuration occurs as a result of HSI, where a critical threshold in the horizontal shear profile is exceeded and a vortex sheet breaks down into individual vortical structures. Following M17, simplifications of the Rayleigh ($\partial^2 \bar{u} / \partial y^2$) and Fjortoft [$(\bar{u} - u_i) \partial^2 \bar{u} / \partial y^2$] criteria were used as proxies for evaluating the role of HSI in misovortex formation. In the context of IOP4, \bar{u} is the domain-averaged east–west component of

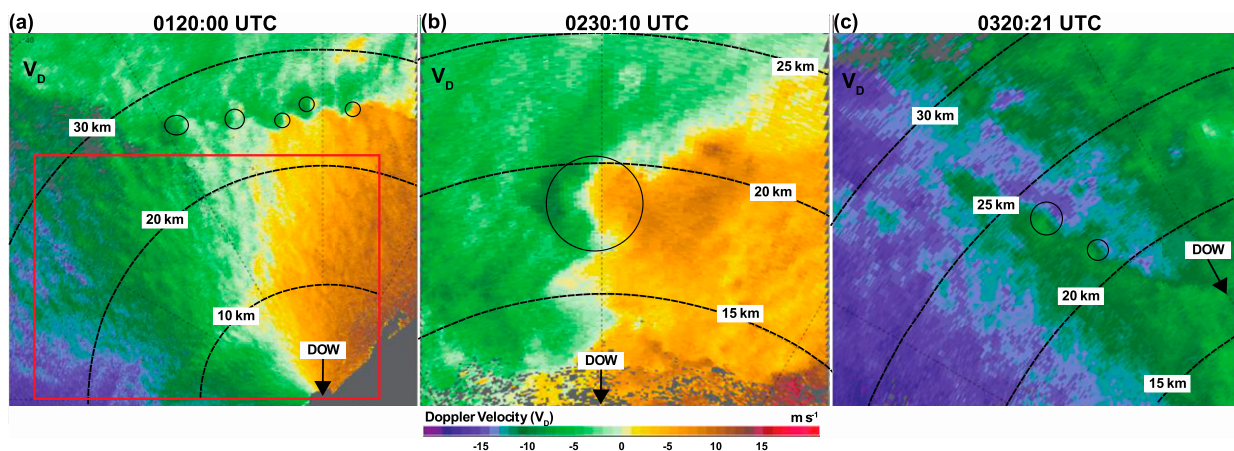


FIG. 8. Example of structures observed in Doppler velocity (V_D) during IOP4: (a) linear streaks with cyclonic misovortices, (b) vortex > 1.5 km in diameter, and (c) anticyclonic vortices. The time of observation is indicated at the top of the panel and direction of the DOW in each panel is labeled and indicated with an arrow. Vortices are annotated with circles. The region of linear streaks is denoted in (a) by the red rectangle.

horizontal velocity, u_i is the value of \bar{u} at the inflection point in the \bar{u} profile, and v is the north–south distance, perpendicular to \bar{u} . Both of these are necessary, but not sufficient, conditions for HSI. Since these criteria contain second-order derivatives of dual-Doppler-derived velocities, the results can be noisy, but pronounced inflections in the profiles occur coincident with the misovortex line (Fig. 13), supporting the hypothesis that, as in M17, HSI was a contributor to misovortex genesis.

HSI is not the only mechanism that can generate misovortices; tilting of horizontal vorticity into the vertical (hereafter “tilting”) may also contribute. Tilting often is difficult to resolve in dual-Doppler analyses, because the near-surface horizontal variations in the vertical velocity are not well captured by distant radars (e.g., Wurman et al. 2007; Wurman et al. 2010; Kosiba et al. 2013). The small grid constructed between 0550 and 0600 UTC for IOP4 may be able to resolve gradients in the low-level vertical velocity due to the proximity of the band to the radars, and as a result, yielded observations closer to the surface (Fig. 14). Between 0550 and 0600 UTC, there were regions of tilting proximal to several of the vertical vorticity centers, analyzed above the background noise. For comparison, the same calculations were performed with the standard grids, both from 0520 to 0530 UTC and from 0550 to 0600 UTC (not shown). During the 0520–0530 UTC period, when only the standard grids were available, there was no discernable tilting analyzed above the noise, but between 0550 and 0600 UTC, the tilting trend, albeit of a lesser magnitude, was similar to what was depicted in the small grid. This positive relationship between tilting and vertical vorticity between 0550 and 0600 UTC suggests that

tilting may have had some role in misovortex genesis and/or maintenance. But, despite the low-level coverage and finescale resolution, without a time history of the relative contributions of tilting and stretching to the total vertical vorticity budget, the exact role of tilting is difficult to discern with the present data. And, while no identifiable regions of tilting were present in the earlier analyses (0520–0530 UTC), the data may be too coarse and/or too high above ground level to capture the necessary gradients needed to calculate tilting. Additionally, horizontal vorticity ahead of the snowband likely was not sufficiently captured due to the lack of clear air scatterers, which, in turn will impact the calculation of tilting and its relative contribution to vertical vorticity.

The vertical vortex structures resolved in Fig. 11 suggest that the misovortices formed on the ascending branch of a secondary circulation (e.g., Ballentine et al. 1998; Bergmaier et al. 2017), with variations in circulation strength at individual vortex locations. Using airborne data from the University of Wyoming King Air and model simulations, Bergmaier et al. (2017) investigated the structure of a secondary circulation that occurred within an intense LLAP precipitation band during OWLeS IOP2b. While not the focus of their investigation, misovortices did occur during IOP2b, but not coincident with the < 1 h of analyzed airborne observations. They concluded that the secondary circulation, forced by horizontal buoyancy gradients, contributed to enhanced updraft motion and was reinforced by latent heat release in the updraft. M17 also examined the secondary circulation wind structure, but only analyzed one vortex at one time, so generalizations about the relationship to the line of misovortices cannot be made.

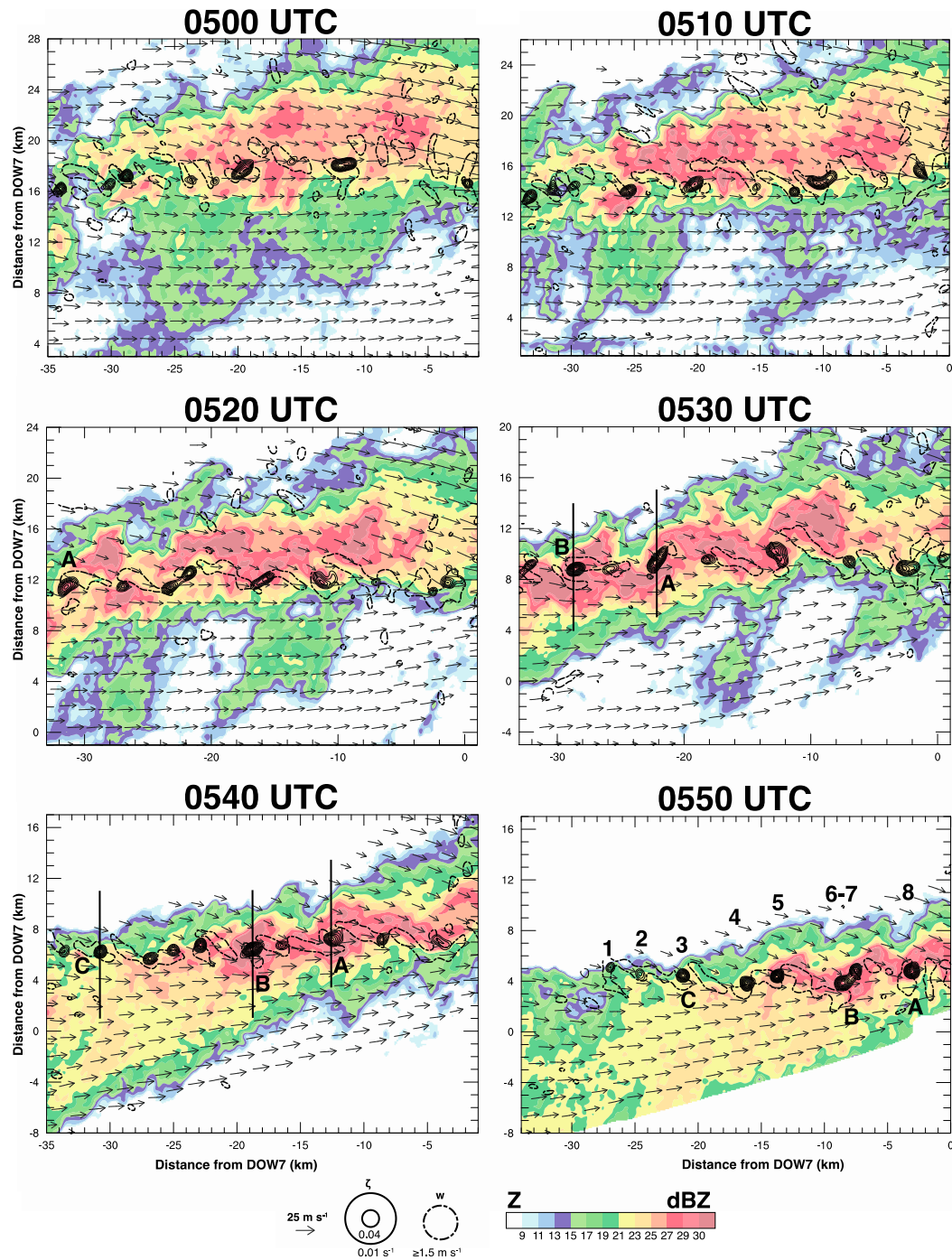


FIG. 9. Dual-Doppler analyses for the standard domain every 10 min between 0500 and 0550 UTC. Analyses are shown at a height of 400 m above radar level (ARL). Color fill depicts radar reflectivity; black line contours depict positive vertical vorticity, contoured from 0.01 to 0.04 s^{-1} every $0.25 \times 10^{-2} s^{-1}$; and dashed line contours depict positive vertical velocity greater than or equal to $1.5 m s^{-1}$. Vectors are ground-relative and depict the horizontal winds. Black lines indicate the locations of vertical cross sections shown in Figs. 11 and 12.

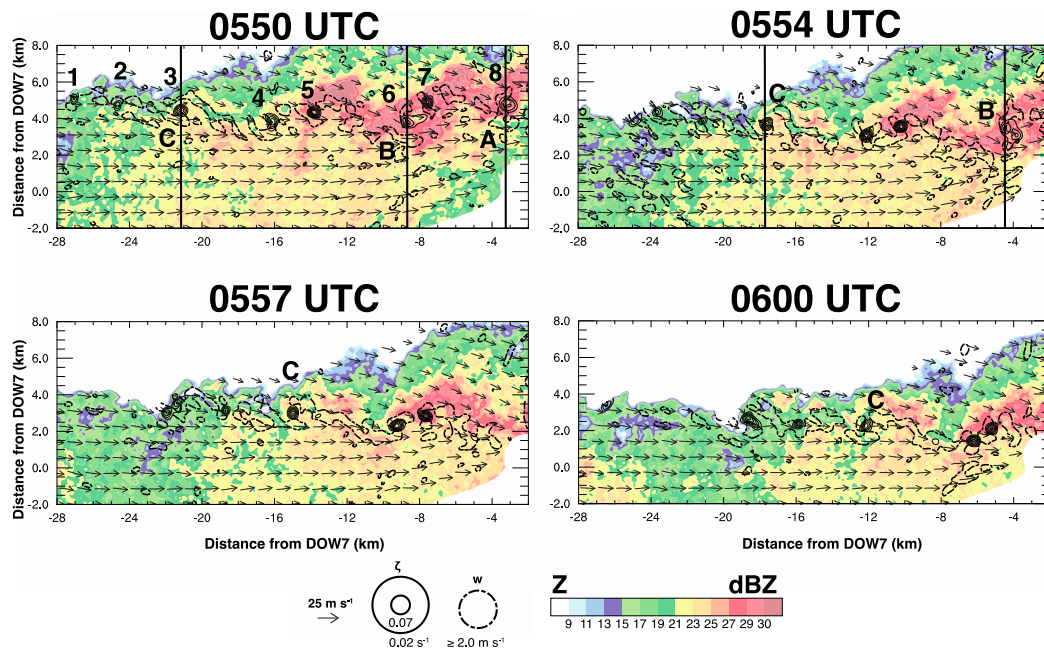


FIG. 10. Dual-Doppler analyses for the small domain every 3–4 min between 0550 and 0600 UTC. Analyses are shown at a height of 400 m ARL. Color fill depicts radar reflectivity; black line contours depict positive vertical vorticity, contoured from 0.02 to 0.07 s^{-1} every 0.01 s^{-1} ; and dashed line contours depict positive vertical velocity greater than or equal to 2.0 m s^{-1} . Vectors are ground-relative and depict the horizontal winds. Black lines indicate the locations of vertical cross sections shown in Figs. 11 and 12.

The inferred buoyancy gradient associated with the secondary circulation implied that different air masses reside on either side of the misovortex line. To determine if parcels from the different air masses comprised the misovortices, trajectories were calculated. Since backward trajectories are more prone to numerical errors (e.g., Dahl et al. 2012), forward trajectories were calculated for the 0520–0530 UTC and 0550–0600 UTC periods using a fourth-order Runge–Kutta scheme at 20-s time steps starting from a height of 200 m ARL. Trajectories were calculated every 200 m. Data were advected forward in time to account for the evolution of the flow field. While there is no strict rule about the interpolation time-step, past studies (e.g., Marquis et al. 2007; Markowski et al. 2012; Kosiba et al. 2013) and sensitivity tests to different interpolation intervals informed the choice of a 20-s time step.

During both time periods, trajectory analyses suggested that air entered the vortices from proximate locations both north and south of the vorticity centers, although parcels entering from south of a vortex were more likely to encounter an updraft and rise upward before potentially becoming ingested in the vortex (Fig. 15). Since the parcels enter the vortices from north and south, it is likely that two different air masses are being drawn into the misocyclones. This type of trajectory path also supports HSI as the primary misovortex

genesis mechanism since there were no abrupt low-level vertical excursions of the parcels near the surface; instead, the parcels converged as they ascended. But, as shown earlier, there were extremely localized regions of tilting proximal to several of the vorticity centers, which would be difficult to capture in the trajectory analysis.

Since the misovortices represent a departure from the background winds, they may contribute to the turbulent kinetic energy (TKE), which will impact the distribution of heat and momentum in these bands (e.g., Kosiba and Wurman 2014) and feedback into precipitation amounts. TKE, approximated as $(1/2)(u'^2 + v'^2 + w'^2)$, where the prime indicate perturbation winds, was calculated for each grid point at $z = 400$ m above radar level (ARL). The u' , v' , and w' winds were derived by subtracting the domain-averaged u , v , and w winds, respectively, from the derived u , v , and w winds at each grid point. Analyses at 0520, 0530, 0540, and 0550 UTC are shown in Fig. 16. The TKE values associated with some of the misovortices were in excess of $20 \text{ m}^2 \text{ s}^{-2}$, were maximum early, and decreased with time. The 0520 and 0530 UTC times had better dual-Doppler coverage both north and south of the vortices, so some of the difference in areal coverage of TKE may be a function of the data coverage. Examination of Doppler spectrum width, a proxy for turbulence (e.g., Istok and Doviak 1986), showed larger spectrum width values

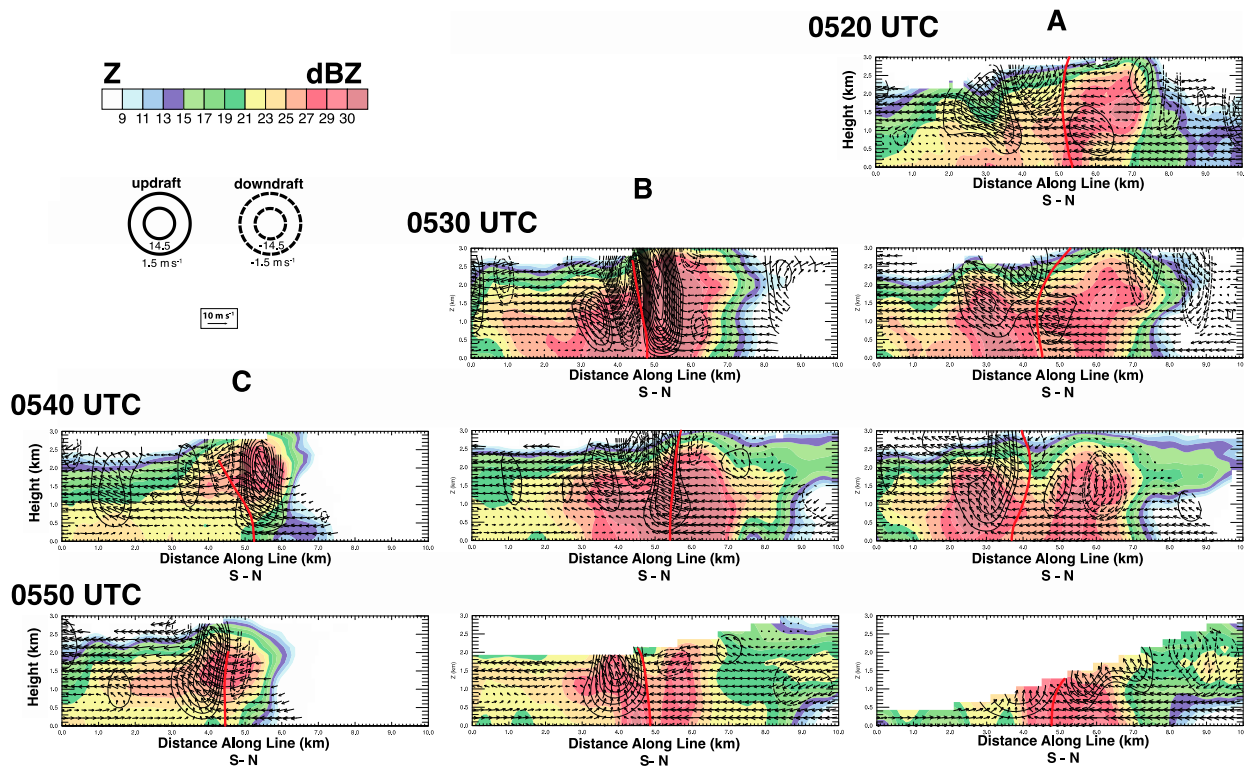


FIG. 11. Vertical cross sections through vortices (right) A, (center) B, and (left) C. Vertical cross sections are along the south–north horizontal lines shown in Figs. 9 and 10. All cross sections are from the standard grid. Colored fill depicts radar reflectivity; solid black line contours depict positive vertical velocity, contoured from 1.5 to 14.5 m s⁻¹, every 1 m s⁻¹; dashed black line contours depict negative vertical velocity, contoured from -1.5 to -14.5 m s⁻¹, every 1 m s⁻¹. The red vertical lines depict the location of the maximum vertical vorticity. Vectors are ground-relative and depict the cross-band vertical wind structure.

associated with the misovortex line (Fig. 17), corroborating the TKE analysis.

c. LLAP band thermodynamic structure

Additional insight on misovortex genesis and evolution can be extracted from thermodynamic observations as parts of the snowband made landfall. There were no temperature measurements over the lake, but inferences about air mass properties can be made prior to, during, and after the snowband traversed the surface weather stations. This allowed, for the first time, examination of the surface thermodynamic properties, in addition to the kinematic causes discussed above, which can influence precipitation production and vortex intensity. Prior to the snowband reaching the DOW7/Pod I location, the Pod I 1-min averaged temperature showed a relatively steady temperature of approximately -3.3°C between 0524 and 0553 UTC (Fig. 18), which corresponded to westerly winds at the DOW7/Pod I location (Fig. 7b). This is ahead (south) of the misovortex line and likely was representative of warm air advection from the comparatively warmer near-surface temperatures over Lake Ontario. Between 0553 and

0556 UTC there was a small-scale decrease in temperature to -4.0°C, followed by an increase in temperature to approximately -3.2°C, which remained relatively steady from 0601 to 0620 UTC. The decrease in temperature from 0553 to 0556 UTC corresponded to the arrival of the leading (southern) edge of the snowband, followed by the passage of the misovortex line at ~0606 UTC (Fig. 4d). Near this time, the wind began to shift from westerly (~270°) to more northerly (~340°) (Fig. 7b). After 0620 UTC, the snowband was south of the Pod I location and the temperature steadily decreased until the end of the temperature record. The final temperature decrease likely was associated with the cold air mass of the Arctic front.

The temperature history from Pod H, which was located ~6.36 km at 232° azimuth from DOW7/Pod I, was slightly different than the Pod I measurements (Fig. 18). This was due, in part, to the snowband orientation and evolution relative to Pod H as well as the upstream differences in the exposure and fetch. Pod I was located at the shoreline, with an immediate upstream fetch over Lake Ontario for northerly and westerly winds. Pod H was 0.17 to 0.30 km from the shoreline, and, depending

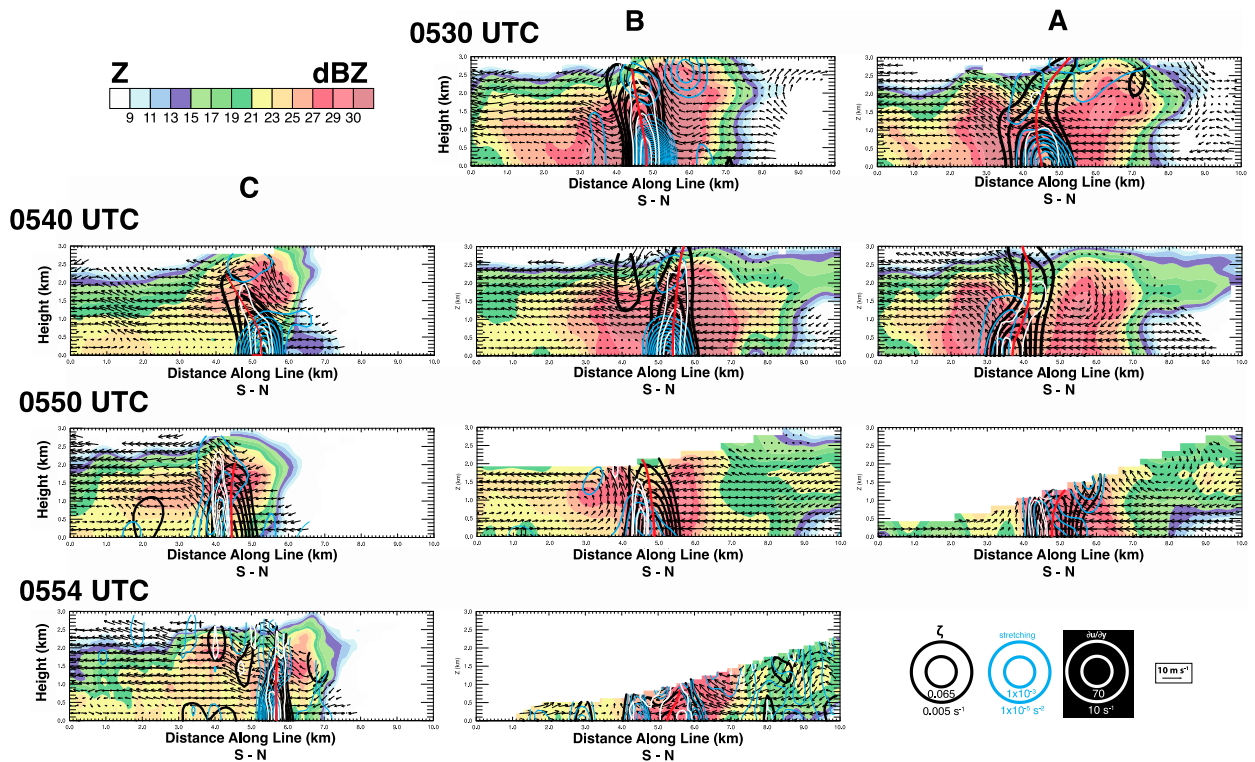


FIG. 12. Vertical cross sections through vortices (right) A, (center) B, and (left) C. Vertical cross sections are along the south–north horizontal lines shown in Figs. 9 and 10. The 0530, 0540, and 0550 UTC cross sections are from the standard grid; the 0554 UTC cross sections use the small grid. Colored fill depicts radar reflectivity; black line contours depict positive vertical vorticity, contoured from 0.005 to 0.065 s^{-1} every 0.05 s^{-1} ; blue contours depict stretching from 1×10^{-5} to $1 \times 10^{-3} \text{ s}^{-2}$, contoured every $2 \times 10^{-5} \text{ s}^{-2}$; white contours depict du/dy from 10 to 70 s^{-1} , contoured every 10 s^{-1} . The red vertical lines depict the location of the maximum vertical vorticity. These vertical vorticity lines are the same as shown in Fig. 11. Vectors are ground-relative and depict the cross-band vertical wind structure.

on the wind direction, was more sheltered by nearby trees and scrub (Fig. 1). But, similar trends were observed with the passage of the misovortex line and the passage of the snowband. DOW6 data indicated that the snowband arrived at the Pod H location at ~ 0600 UTC, but the line of misovortices did not impact Pod H until much later, around 0628 UTC. Similar to DOW7/Pod I, at about the time, the misovortex line impacted Pod H, and the wind shifted from westerly to more northerly. Also, the temperature increased around 0628 UTC and remained relatively constant at -4.2°C until ~ 0637 UTC, when it then decreased to -4.8°C and remained approximately constant until the end of the observation period (Fig. 18). The misovortex line remained north of Pod H for almost 20 min longer than at the DOW7/Pod I location. As a result, warming occurred 20 min later at Pod H, when the misovortex line passed over Pod H's location. In contrast, the misovortex line impacted the DOW7/Pod I location ~ 10 min after the arrival of the leading edge of the reflectivity band.

The temperature history from both Pods I and H suggested that the vortices were located near a baroclinic

zone, with slightly cooler air just south of the vortices and slightly warmer air just north of the vortices. Since Pod H didn't observe a temperature increase until after the passage of the misovortex line, despite being located within the precipitation band since ~ 0600 UTC, it is surmised that the warming was associated with the misovortices. While it is not possible from the observations to diagnose definitively what processes were responsible, downward transport of air observed in the dual-Doppler fields (see several panels in Fig. 12) north of the vortices, slightly warmed by latent heat release enhanced by the misovortices, may have contributed the warming. As diagnosed from enhanced TKE and larger values of spectrum width, the misovortices likely were indicative of enhanced mixing. As shown in the trajectory analysis, the air that comprised the misovortices came from both south and north of the misovortices' locations, which suggested that mixing of different air masses occurred.

d. LLAP band precipitation structure

The analyses presented above suggest that the misovortices may alter the precipitation intensity through

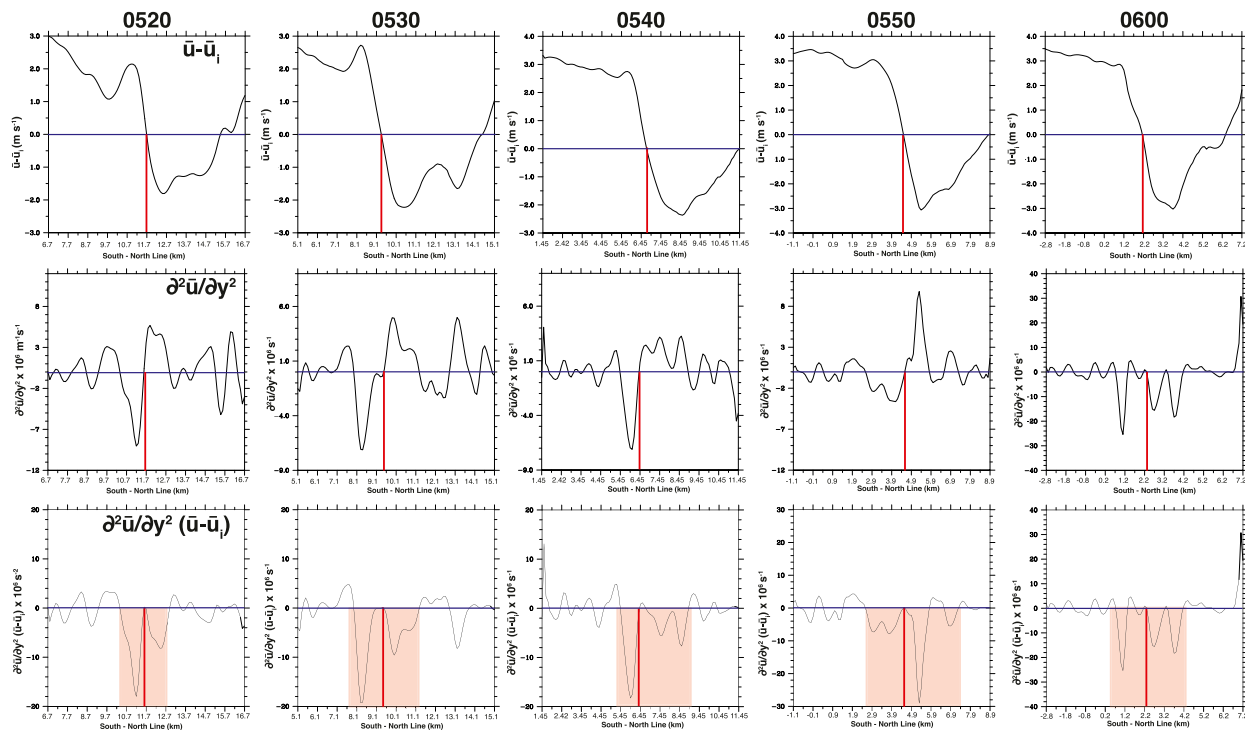


FIG. 13. Instability criteria evaluated perpendicular to the misovortex line from 0520 to 0600 UTC. The 0600 UTC time uses the small grid. The x axis is the south–north coordinates along a 10-km line centered on the inflection point (u_i) shown in the top row. The distances correspond to the dual-Doppler grids in Figs. 9 and 10. The red lines mark the location of the inflection point and the blue lines denote the zero line for the instability parameters. The shaded red region in the bottom row highlights the area where Fjortoft’s instability criterion is satisfied.

mixing and latent heat release. Throughout IOP4, the DOW 6 and 7 differential reflectivity (Z_{DR}) fields were relatively flat, with values approximately zero coincident with the higher reflectivity areas associated with the snowband(s) and slightly more variable along the low reflectivity horizontal and vertical edges. As revealed by

both the sounding data and the DOW copolar cross-correlation coefficient (ρ_{hv}) field, there was no melting layer, so only frozen precipitation was expected. Comparison to closest WSR-88D (Montague, NY; KTYX) revealed a similar Z_{DR} and ρ_{hv} fields. Using the SUNY sounding from 0459 UTC, hydrometeor identification algorithms (Vivekanandan et al. 1999), specific to the radar frequency, were applied to both the X-band DOW and the S-band KTYX data. Retrievals from the DOWs and KTYX indicated that the band was comprised mainly of “dry snow” at all times, with the periphery of the band comprising snow crystals (Fig. 19). No surface verification of hydrometeor type was available when the band was over the lake, but observations by participants stationed at SUNY Oswego and by proximate instrumentation indicated that dendrites were the predominate hydrometeor type as the band made landfall around 0550 UTC. Admittedly, the hydrometeor identification likely was strongly influenced by the lack of melting, so how it performs in a more complex thermodynamic lake-effect precipitation environment has yet to be tested.

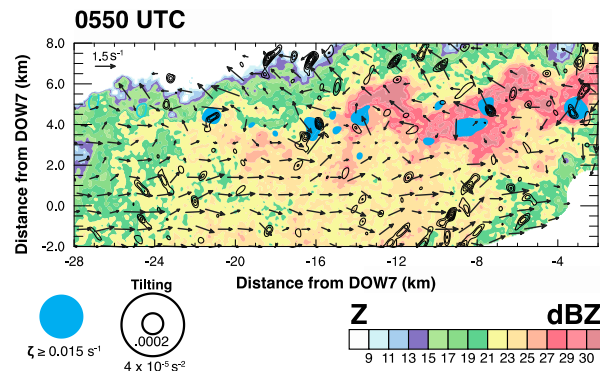


FIG. 14. Horizontal vorticity (vectors), vertical vorticity (cyan shading), reflectivity (color contours), and tilting (black line contours) for the small grid at $z = 400$ m ARL. Tilting is contoured from 4×10^{-5} to $2 \times 10^{-4} \text{ s}^{-2}$ every $2 \times 10^{-5} \text{ s}^{-2}$. Vertical vorticity, ζ , greater than or equal to 0.015 s^{-1} is shaded in cyan.

The misovortices were associated with high reflectivity, so, as expected, higher precipitation rates were

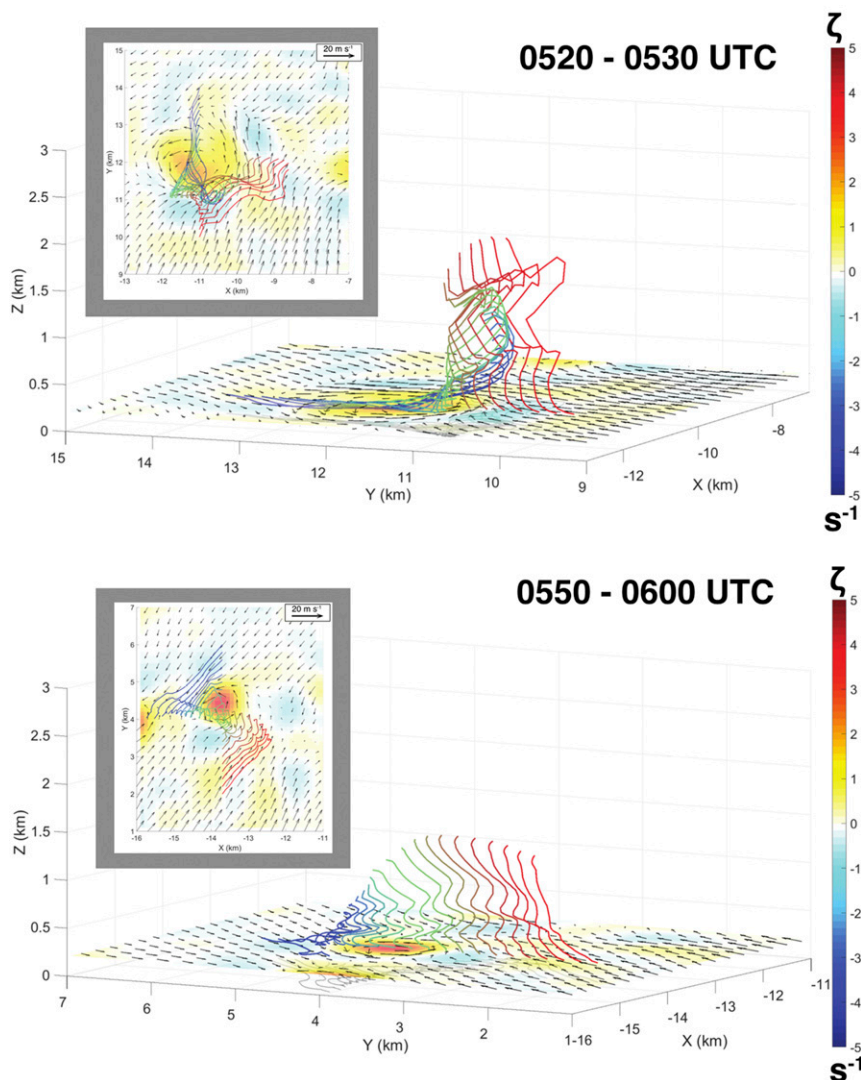


FIG. 15. Forward trajectories starting at (top) 0520 UTC and ending at 0530 UTC and starting at (bottom) 0550 UTC and ending at 0600 UTC. Vertical vorticity ($\times 100 s^{-1}$) is color contoured; horizontal winds are represented by the vectors; trajectories are the colored lines. The trajectories all start at $z = 200$ m ARL. The trajectories that comprise the misovortex come from north and south of the circulation center.

associated with those structures (Fig. 19). Visual observations from OWLeS participants stationed at the SUNY Oswego sounding location indicated that at ~ 0540 UTC the snowfall began to increase and over the next ~ 30 min “there was moderate to heavy snow and white out conditions” and then, by 0615 UTC, “there were just snow flurries.” During this short observation interval, the measured snowfall total at SUNY Oswego was 1.9 cm. As the snowband made landfall, the gustiness, coupled with a narrow band structure precluded attributing local maximums to any particular misovortex. But, when compared to earlier observations, the highest reflectivities occurred coincident with the misovortices.

Observations by Steiger et al. (2013) and M17 suggest a similar relationship.

e. In situ misovortex surface observations

As the snowband made landfall near Oswego, both the DOW7 and Pod I barometers recorded a sharp, small-scale decrease in pressure of ~ 1.4 mb within the generally upward pressure trend (Fig. 20). Examination of DOW7 velocity data around the pressure decrease suggested that this pressure perturbation was due to a proximal passage of a misovortex at the DOW7/Pod I location (Fig. 21a). The vortex line had a predominantly eastward propagation speed of $\sim 15 m s^{-1}$, so using the 0605:30 UTC

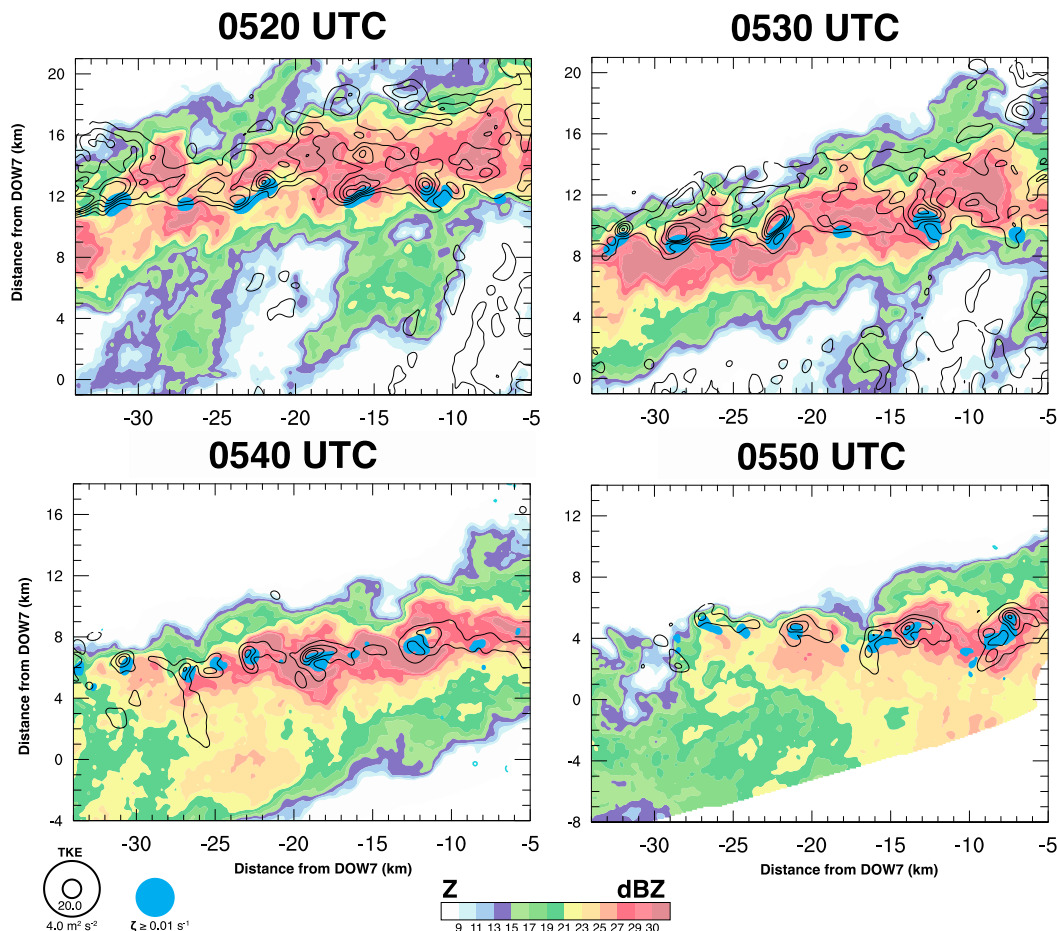


FIG. 16. Turbulent kinetic energy (black line contours), vertical vorticity (cyan color fill), and reflectivity (color contours) shown at $z = 400$ m for the standard grid every 10 min from 0520 to 0550 UTC. Turbulent kinetic energy, TKE, is contoured from 4.0 to $20.0 \text{ m}^2 \text{ s}^{-2}$, every $4.0 \text{ m}^2 \text{ s}^{-2}$. Vertical vorticity, ζ , greater than or equal to 0.01 s^{-1} is shaded in cyan. The largest values of TKE are proximal to the misovortices.

DOW7 sweep, which corresponded to a beam time of 0605:37 UTC at the vortex location, the misovortex was ~ 500 m from DOW7; the vortex should have impacted the DOW7 location $\sim 0606:10$ UTC, consistent with the DOW7 pressure time series. A similar pressure perturbation was observed later, at 0628:51 UTC, by Pod H (Fig. 20), which was farther south and slightly more inland. DOW7 data were blocked over the Pod H location, but DOW6 data near that time corroborated the passage of a misovortex (Fig. 21b). Comparable trends were observed when a misovortex passed over a surface station near the shore of the Sea of Japan (Inoue et al. 2016).

f. Discussion

To date, the only other dual-Doppler analysis of a misovortex-containing snowband was presented by M17, who also utilized a numerical simulation of the same event (IOP7) in order to gain additional insight into band and misovortex processes. Similar to IOP7, the vortices

in IOP4 formed along a cyclonic shear zone, dual-Doppler derived² vertical vorticity values were $\sim 0.03 \text{ s}^{-1}$ and had diameters 1–3 km. In both the dual-Doppler analyses of IOPs 4 and 7, and in the numerical simulation of IOP7, vertical vorticity was maximized in the lowest 1 km. Analyses of both IOPs supported the hypothesis that HSI contributed to misovortex formation, but the availability of low-level radar data³ and some thermodynamic data for IOP4 suggest that misovortex genesis enhanced by baroclinic instability and maintenance may be aided by tilting.

Unlike in IOP7, the misovortices did not stay in the same band-relative location throughout IOP4, and,

² Exact values vary between IOPs likely due to the choices in objective analysis parameters.

³ Two of the low-level tilts from one of the radars were unavailable.

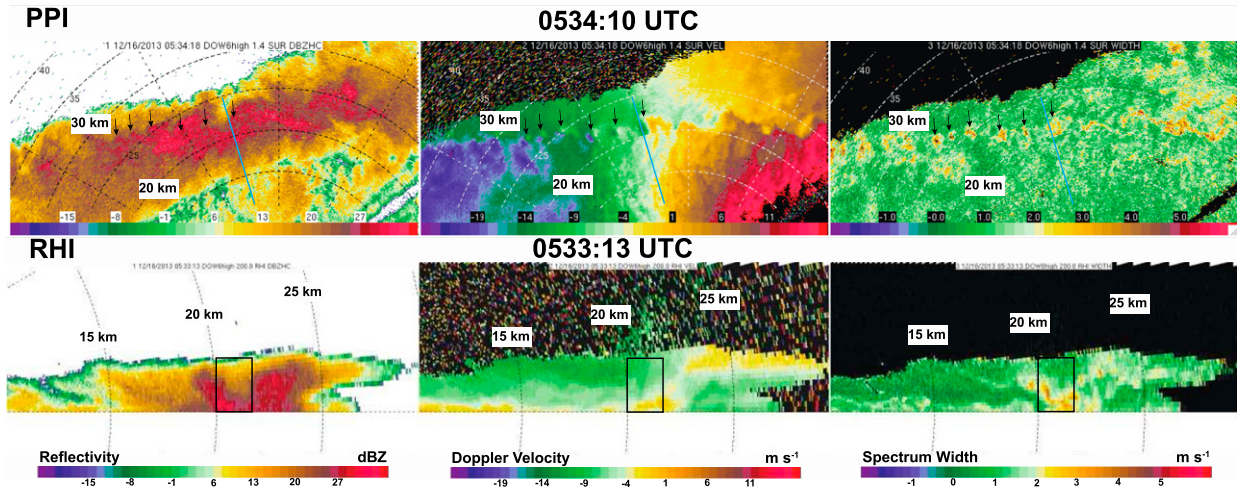


FIG. 17. (left) Radar reflectivity, (center) Doppler velocity, and (right) spectrum width from DOW6. (top) Fields from a PPI scan and (bottom) fields from an RHI scan closest in time to the PPI. The blue line in the PPIs depicts the location of the RHIs. The black arrows in the top panels mark the location of misovortices. The black rectangles in the bottom panels denote the location of the misovortex transected by the blue line. Enhanced spectrum width occurs with the misovortices, suggesting an enhancement of turbulent kinetic energy.

specifically during the ~1-h analysis period. This shift in location appeared to be due, in part, to the interaction of the band with the Arctic front, which shifted the convergence zone relative to the band. Prior to 0340 UTC the convergence zone was south of the band, as the band outflow interacted with the downstream environment, but as the band became increasing more under the direct influence of the Arctic front, the misovortices shifted

north where convergence and, potentially thermal gradients, were maximized.

4. Multisnowband misovortex characteristics

IOP4 was an exemplary case for dual-Doppler analysis and, with onshore thermodynamic observations, provided additional insights regarding the kinematic

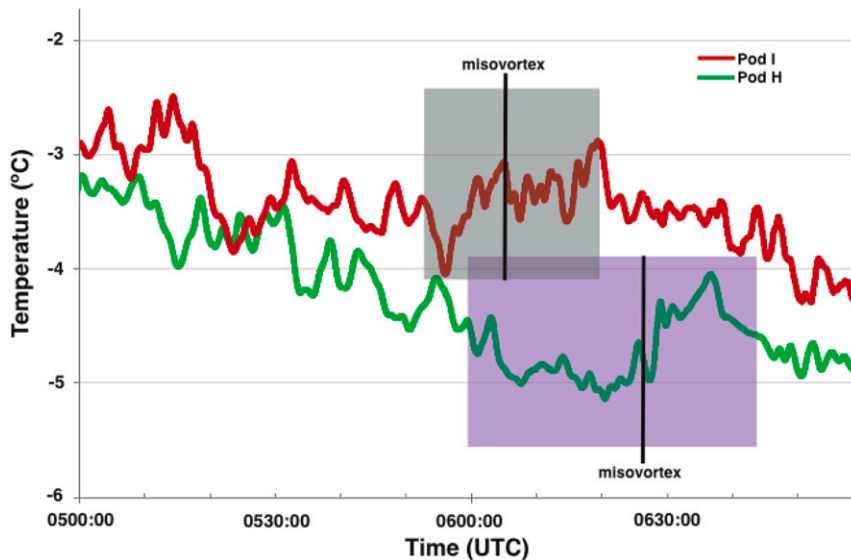


FIG. 18. The 1-min averaged temperature observations from the Pod I (red) and Pod H (green) 0500 to 0700 UTC 16 Dec. The snowband passage is denoted by the gray shading over Pod I and by the purple shading over Pod H. The time of misovortex passage is labeled with a black vertical line. The snowband first passed over Pod I and then over Pod H.

DOW7

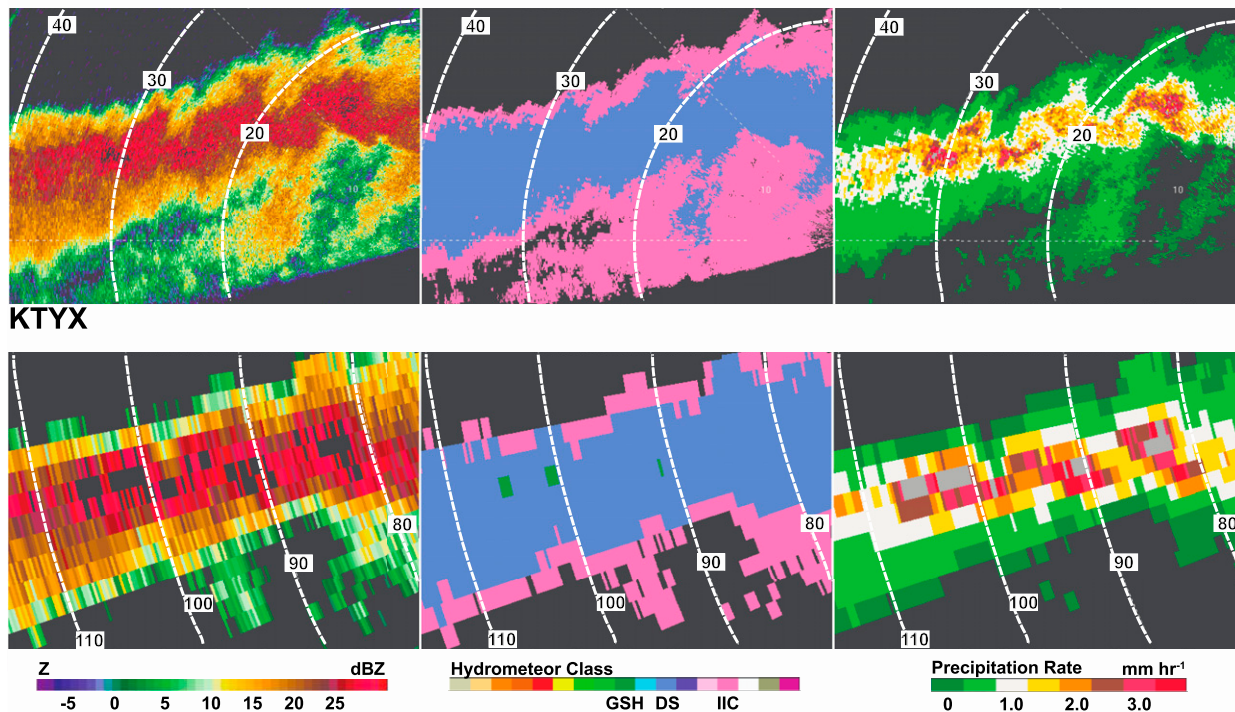


FIG. 19. Comparison between (top) DOW7 and (bottom) KTYX derived (middle) hydrometeor type and (right) precipitation rate at 0530 UTC 16 Dec 2013. (left) The radar reflectivity field from each radar is shown for context. The hydrometeor classes are as follow: GSH is graupel or small hail; DS is dry snow; and IIC is irregular ice crystals. The snowband is predominantly dry snow, with ice crystals along the periphery. Range rings from each radar are shown every 10 km.

properties of a misovortex-containing LLAP band beyond other studies. While it is beyond the scope of this manuscript to do an in-depth analysis of all of the individual misovortices sampled during OWLeS, the OWLeS dataset provides the opportunity to compile statistics from snapshots of misovortex characteristics for a large sampling of snowbands, akin to a seasonal or project “census”, and evaluate how the misovortex kinematics deduced for the IOP4 snowband fit into the larger spectrum of OWLeS-observed misovortices.

To do so, DOW data from the twelve OWLeS LLAP IOPs were manually perused for the existence of coherent vortices. Coherent was defined as an organized structure, where a clear vortex couplet was identifiable. Misovortices were observed in eleven of the twelve LLAP events (IOPs 2, 3, 4, 5, 7, 9, 15, 19, 20, 21, and 22). Single DOW data from the IOPs⁴ were used to compile information on vortex strength, quantified by ΔV , diameter, and spacing between vortices. For each IOP, the mean, median, and mode, binned by 1 ms^{-1} , 0.1, and

0.5 km increments, respectively, vortex characteristics were compiled every 10 min using the lowest unblocked elevation angle, either 0.5° or 1.0° . This resulted in 1334 vortex observations from DOW6 and 2163 vortex observations from DOW7. To account for any potential sampling differences between the radars for a given IOP, DOW 6 and 7 statistics were calculated individually for each radar as well as for all of the 10-min vortex observations. Since no significant differences were found between the individual-radar and combined statistics, the discussion focuses on the combined findings. It is important to note that this approach does not track individual misovortices, but instead compiles a snapshot of the characteristics of the misovortices that exist at each 10-min interval. As a result, throughout an IOP, some misovortices may be sampled more than once, and at different phases in their evolution, and some misovortices may not be sampled at all since they only exist between 10-min sampling intervals. But, a spot check of three different IOPs suggest that the opposing-sign errors of multiple- and undercounting are minor.

Figure 22 depicts the distribution of strength, diameter, and spacing of the misovortices sampled during OWLeS. The mean spacing between the sampled

⁴For IOPs 19, 21, and 22 (7 and 20) only DOW7 (DOW6) data are available.

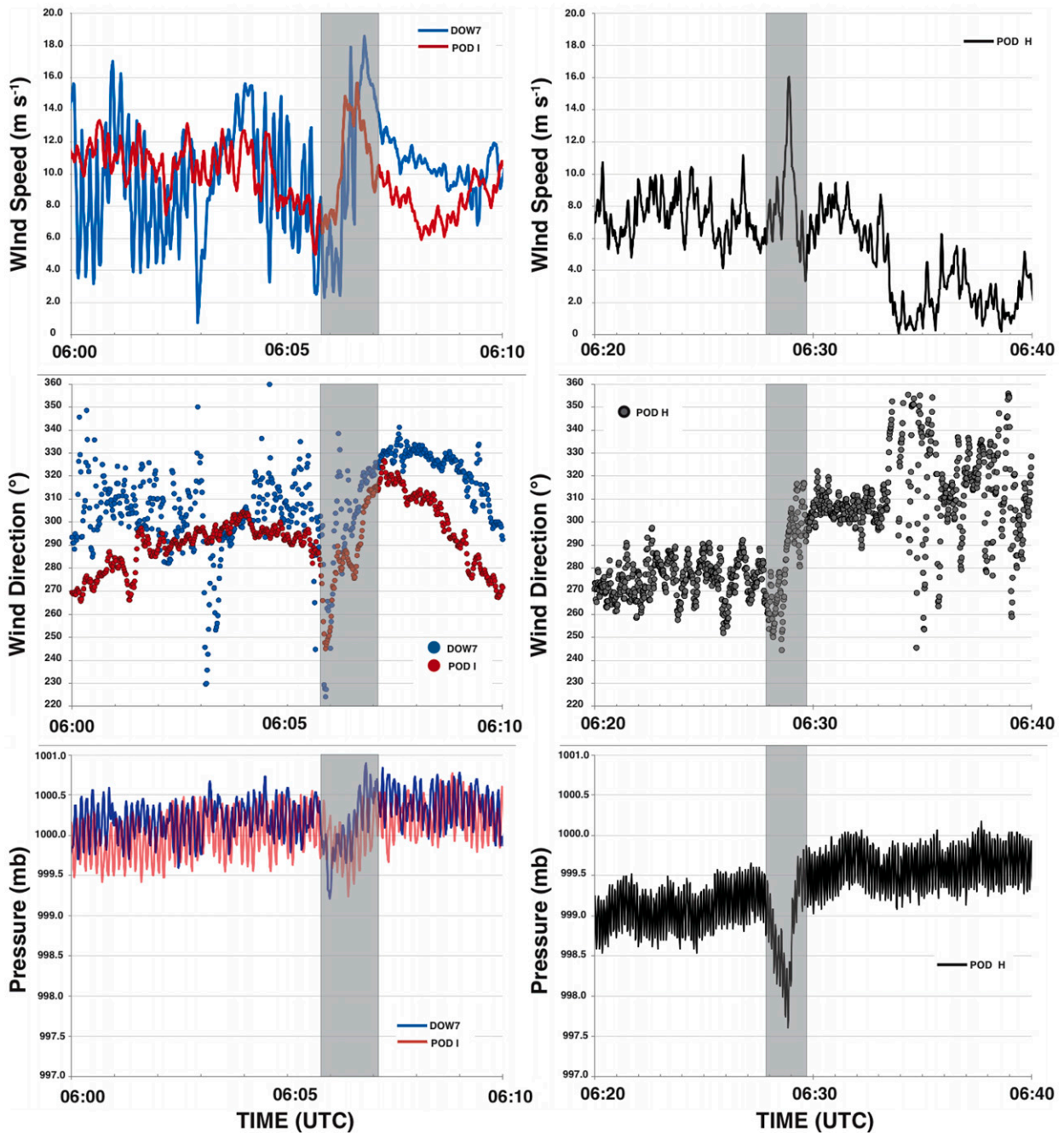


FIG. 20. Time series of the misovortex passage (gray shading) at (left) DOW7 and Pod I and at (right) Pod H. Shown are (top) wind speeds in m s^{-1} , (middle) direction in degrees, and (bottom) pressure in mb.

misovortices was 3.2 km, with a standard deviation of 2.0 km; the median spacing was 2.8 km; the mode spacing was 2.0 km. The mean strength for all the cyclonic vortices sampled was 11.4 m s^{-1} , with a standard deviation of 4.1 m s^{-1} ; the median strength was 10.7 m s^{-1} ; the mode strength was 10.0 m s^{-1} . The mean diameter for all the cyclonic vortices sampled was 0.95 km, with a

standard deviation of 0.75 km; the median diameter was 0.77 km; the mode diameter was 0.50 km. Correspondingly, the mean inferred vertical vorticity was 0.039 s^{-1} ; the median inferred vertical vorticity was 0.028 s^{-1} ; the mode inferred vertical vorticity was 0.020 s^{-1} . There was no correlation between vortex diameter and strength (not shown). Vertical vorticity values were significantly less

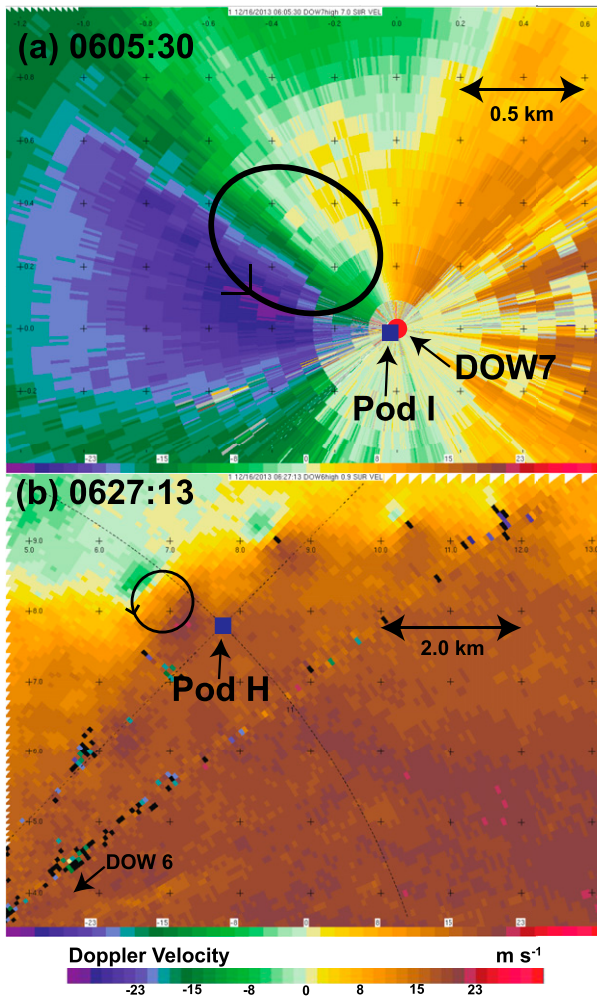


FIG. 21. (a) DOW7 Doppler velocity of the misovortex couplet closest in time to the vortex passage at the DOW7 and Pod I location. Surface data show a decrease in pressure and an increase in velocity around 0606 UTC 16 Dec 2013, consistent with the annotated vortex traveling at $\sim 15 \text{ m s}^{-1}$ and transiting the DOW7/Pod I location. (b) DOW6 Doppler velocity data closest in time to the passage of a misovortex over Pod H. Surface data show a decrease in pressure and an increase in velocity around 0629 UTC 16 Dec 2013, consistent with the annotated vortex traveling at $\sim 15 \text{ m s}^{-1}$ and transiting the Pod H location.

than the $0.2\text{--}2 \text{ s}^{-1}$ values typically observed in supercell tornadoes (e.g., Wurman et al. 1996; Wurman et al. 2007; Marquis et al. 2008; Wurman et al. 2010; Kosiba et al. 2013) and the $\sim 0.1 \text{ s}^{-1}$ values characteristic of the tornado-scale vortices documented in Hurricane Harvey (Wurman and Kosiba 2018), but slightly larger than the strongest observed convergence line misovortices ($\sim 0.01 \text{ s}^{-1}$) (e.g., Friedrich et al. 2005; Marquis et al. 2007), and similar to the weakest NSTs ($\sim 0.03\text{--}0.07 \text{ s}^{-1}$) (e.g., Wakimoto and Wilson 1989). Although less frequent, anticyclonic vortices were observed in 13% of

the analyzed sweeps (e.g., Fig. 8c). The anticyclonic vortices generally were weaker and smaller than the cyclonic ones. The mean strength was 8.2 m s^{-1} ; the median strength was 8.0 m s^{-1} ; the mode strength was 8.0 m s^{-1} . The mean diameter was 0.54 km ; the median diameter was 0.42 km ; the mode diameter was 0.40 km . Other, less frequently occurring vortical structures, including multiple and mesoscale ($D \geq 3\text{--}4 \text{ km}$) vortices, also were documented (e.g., Fig. 8b). Although difficult to objectively quantify, location within the line often varied in time during an IOP and from IOP to IOP. Differences in the reflectivity morphology were observed – ranging from no discernable shape to hook-like appendages, some even with a low-reflectivity eye, characteristic of some tornadoes (Fig. 23) (e.g., Wurman et al. 1996; Wurman and Kosiba 2013), but, in general, there wasn't an obvious link between a well-defined reflectivity morphology and vortex intensity.

Many of the strongest vortices ($V \geq 23 \text{ m s}^{-1}$; i.e., ≥ 3 standard deviations) occurred during IOP7 (7 January 2014). As mentioned above, a dual-Doppler and modeling analyses of this case was presented in M17. The most intense vortices occurred between 0500 and 0730 UTC, along the northern periphery of the band (see M17 Fig. 6). There were several times when more than one vortex with $\Delta V \geq 23 \text{ m s}^{-1}$ was present (e.g., 0513, 0633 UTC). IOP 4 (discussed above) and IOP 22 (28 January 2014) also had vortices with $\Delta V \geq 23 \text{ m s}^{-1}$, but far less numerous than IOP7. In contrast to IOP7, the strong vortices in IOPs 4 and 22 were not confined to just the northern edge of the band. As discussed above, the approaching Arctic front influenced the location of the misovortices in IOP4, which was different from IOP7, so location within a band needs to be evaluated on a case-by-case basis in order to identify the type and influence of mitigating conditions.

Returning to the question of “how does IOP4 fit into the overall misovortex population sampled during OWLeS?”, the intensity, diameter, and spacing all were within the 75th percentile (14 m s^{-1} , 1.2 , and 4.0 km , respectively), but not the 25th percentile (9 m s^{-1} , 0.4 , and 2.0 km , respectively), of all the observations (Fig. 22). The bias of IOP4 to, on average, have slightly “higher-end” misovortices was one of the reasons this case and IOP7 were chosen for dual-Doppler analyses. Vortices were resolved in the DOW data, lending confidence to the analyses presented. While on the higher end of the spectrum, the characteristic vortices from IOP4 did not deviate significantly from OWLeS-observed LLAP cases.

Assuming cyclostrophic balance, the resultant pressure gradient was 1.6 mb km^{-1} for the 75th vortices and 2.0 mb km^{-1} for the 25th percentile vortices. The cyclostrophic balance assumption for the vortex sampled

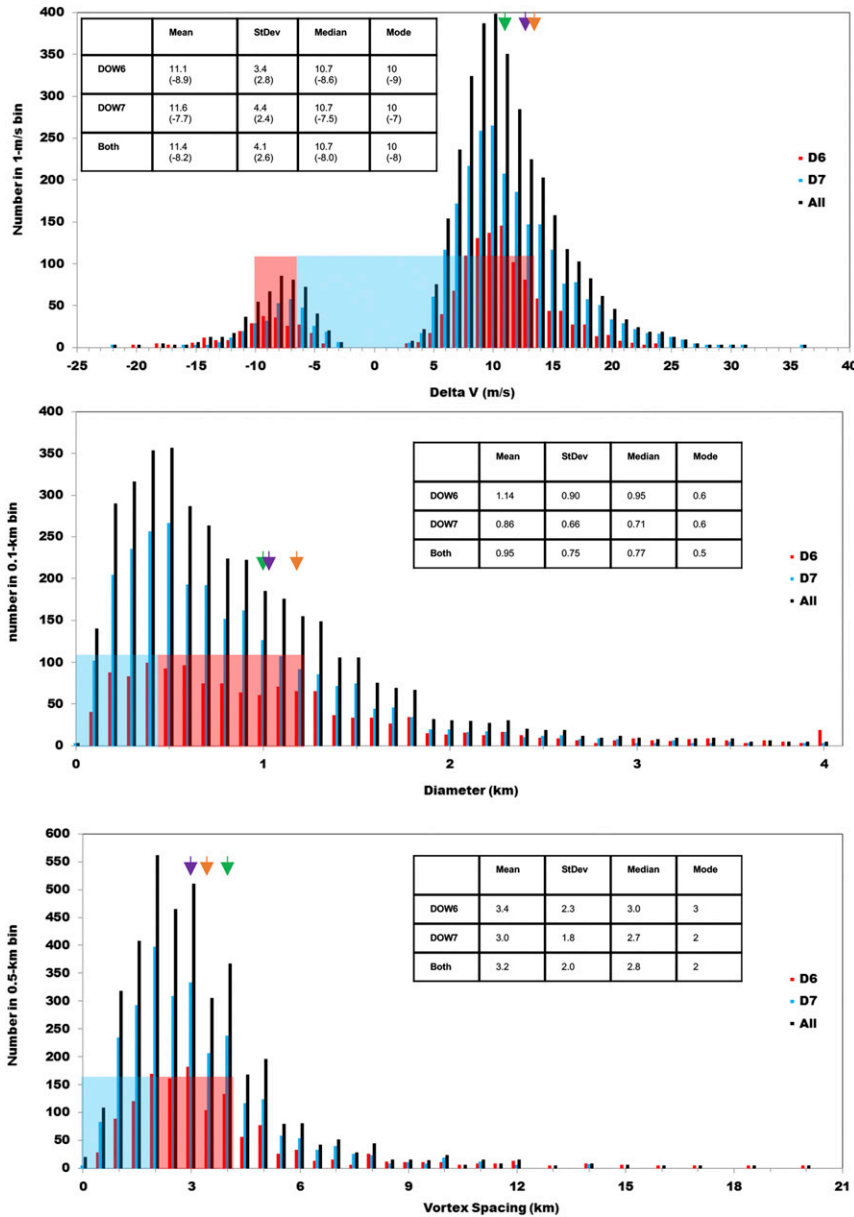


FIG. 22. Histograms of (top) delta-V, (middle) diameter, and (bottom) spacing resulting from the 10-min sampling of misovortices observed in LLAP bands during the OWLeS project. Arrows indicate the values for IOP4, where the green depicts the mode; the orange arrow depicts the mean; and the purple arrow depicts the median. The red shading represents the 75th percentile and the blue shading represents the 25th percentile.

by surface instrumentation during IOP4 would yield a pressure deficit of ~ 2.0 mb, which is ~ 0.6 mb lower than what was measured, but similar to the calculated pressure gradient for the 25th percentile vortices. During the passage of the vortices, the air was approximately saturated and visibility was low, as documented by OWLeS crew, often due to blowing snow. It is possible that snowband misovortices may frequently occur in

opaque environments, similar to tornado-scale vortices in hurricanes, so, unlike NSTs, visible funnels may not be regularly observed in these “typical” events.

5. Conclusions

We have shown that misovortices documented in IOP4 was within the characteristic range of OWLeS-observed

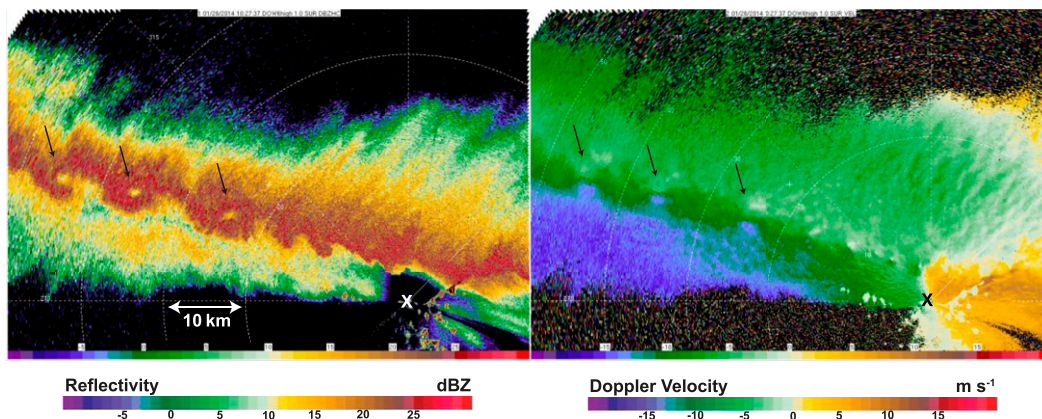


FIG. 23. Example of clear echo “eyes” and hook-shaped appendages associated with misocyclones as observed by DOW6 during IOP19. (left) Radar reflectivity and (right) Doppler velocity. The “X” in each panel indicated the DOW6 location. Arrows denote the vortices with clear echo “eyes.” Dual-Doppler data were not available for this case.

LLAP events. An in-depth analysis of IOP4 suggested that the vortices form as a result of HSI, similar to the findings of M17, and adding to the growing body of evidence that this is likely the mechanism for misovortex formation in LLAP snowbands. Although thermodynamic observations were not available over the lake, DOW7 mesonet and Pods H and I were located near the coastline and suggested that the convergence lines also were located along thermodynamic boundaries. While early on in IOP4 snowband-generated boundaries and likely controlled the location of the vortices, by the end of the IOP, the Arctic front dominated. TKE was enhanced in the vortices, which can influence heat and momentum transport in these bands, and indeed, higher precipitation rates were associated with the misovortices. Modeling studies are needed to evaluate these effects.

Using data from all of the OWLeS LLAP IOPs, it was found that vortices commonly occurred in the LLAP snow events sampled during the project. Most of the vortices are $< \sim 1$ km in diameter and were part of a line. In general, the strength, diameter, and spacing distributions were similar to what was documented in the two-LLAP band climatology of Steiger et al. (2013), the OWLeS case study of M17, and the vortices documented over the Sea of Japan (Inoue et al. 2011; Inoue et al. 2016). While the spacing and diameter were similar to the misocyclones observed in quiescent “warm season” phenomena (e.g., Kingsmill 1995; Friedrich et al. 2005; Arnott et al. 2006; Marquis et al. 2007), the characteristic intensity/vertical vorticity values were slightly larger for the cold season/snowbands. When compared to NSTs (e.g., Wakimoto and Wilson 1989; Kosiba et al. 2014), the vertical vorticity/intensity values for the cold season/snowbands were smaller than all but the weakest NSTs. In all cases, the vertical vorticity was maximized

near the surface. The differences in strength likely were due to the underlying environments, but there does appear to be a favored diameter and spacing for the variety of HSI-generated misovortices observed in the atmosphere.

Acknowledgments. This research was supported by National Science Foundation Grants AGS-1259185 and AGS-1258860. The DOWs and Pods were supported by National Science Foundation Grant AGS-1361237. Thanks to the OWLeS crew for maintaining the instruments and collecting this valuable data in challenging conditions. We thank the editor and the reviewers for their comments, which substantially improved the clarity of the text and figures. The sounding and dual-Doppler plots were created using NCL.

REFERENCES

- Arnott, N., Y. Richardson, J. Wurman, and E. M. Rasmussen, 2006: Relationship between a weakening cold front, misocyclones, and cloud development on 10 June 2002 during IHOP. *Mon. Wea. Rev.*, **134**, 311–335, <https://doi.org/10.1175/MWR3065.1>.
- Ballentine, R. J., A. J. Stamm, E. E. Chermack, G. P. Byrd, and D. Schleede, 1998: Mesoscale model simulation of the 4–5 January 1995 lake-effect snowstorm. *Wea. Forecasting*, **13**, 893–920, [https://doi.org/10.1175/1520-0434\(1998\)013<0893:MMSOTJ>2.0.CO;2](https://doi.org/10.1175/1520-0434(1998)013<0893:MMSOTJ>2.0.CO;2).
- Bergmaier, P. T., B. Geerts, L. S. Campbell, and W. J. Steenburgh, 2017: The OWLeS IOP2b lake-effect snowstorm: Dynamics of the secondary circulation. *Mon. Wea. Rev.*, **145**, 2437–2459, <https://doi.org/10.1175/MWR-D-16-0462.1>.
- Bringi, V., and V. Chandrasekar, 2001: *Polarimetric Doppler Weather Radar: Principles and Applications*. Cambridge University Press, 636 pp.
- Buban, M. S., C. L. Ziegler, E. N. Rasmussen, and Y. P. Richardson, 2007: The dryline on 22 May 2002 during IHOP: Ground radar

- and in situ data analyses of the dryline and boundary layer evolution. *Mon. Wea. Rev.*, **135**, 2473–2505, <https://doi.org/10.1175/MWR3453.1>.
- Byrd, G. P., R. A. Anstett, J. E. Heim, and D. M. Usinski, 1991: Mobile sounding observations of lake-effect snowbands in western and central New York. *Mon. Wea. Rev.*, **119**, 2323–2332, [https://doi.org/10.1175/1520-0493\(1991\)119<2323:MSOOLE>2.0.CO;2](https://doi.org/10.1175/1520-0493(1991)119<2323:MSOOLE>2.0.CO;2).
- CSWR, 2019: Center for Severe Weather Research. Accessed 10 March 2019, <http://www.cswr.org/contents/aboutdows.php>.
- Dahl, J. M., M. D. Parker, and L. J. Wicker, 2012: Uncertainties in trajectory calculations within near-surface mesocyclones of simulated supercells. *Mon. Wea. Rev.*, **140**, 2959–2966, <https://doi.org/10.1175/MWR-D-12-00131.1>.
- Forbes, G. S., and J. H. Merritt, 1984: Mesoscale vortices over the Great Lakes in wintertime. *Mon. Wea. Rev.*, **112**, 377–381, [https://doi.org/10.1175/1520-0493\(1984\)112<0377:MVOTGL>2.0.CO;2](https://doi.org/10.1175/1520-0493(1984)112<0377:MVOTGL>2.0.CO;2).
- Foster, R. C., 2005: Why rolls are prevalent in the hurricane boundary layer. *J. Atmos. Sci.*, **62**, 2647–2661, <https://doi.org/10.1175/JAS3475.1>.
- Friedrich, K., D. E. Kingsmill, and C. R. Young, 2005: Misocyclone characteristics along Florida gust fronts during CaPE. *Mon. Wea. Rev.*, **133**, 3345–3367, <https://doi.org/10.1175/MWR3040.1>.
- , —, C. Flamant, H. V. Murphey, and R. M. Wakimoto, 2008a: Kinematic and moisture characteristics of a non-precipitating cold front observed during IHOP. Part I: Across-front structures. *Mon. Wea. Rev.*, **136**, 147–172, <https://doi.org/10.1175/2007MWR1908.1>.
- , —, —, —, and —, 2008b: Kinematic and moisture characteristics of a nonprecipitating cold front observed during IHOP. Part II: Along-front structures. *Mon. Wea. Rev.*, **136**, 3796–3821, <https://doi.org/10.1175/2008MWR2360.1>.
- Grim, J. A., N. F. Laird, and D. A. R. Kristovich, 2004: Mesoscale vortices embedded within a lake-effect shoreline band. *Mon. Wea. Rev.*, **132**, 2269–2274, [https://doi.org/10.1175/1520-0493\(2004\)132<2269:MVEWAL>2.0.CO;2](https://doi.org/10.1175/1520-0493(2004)132<2269:MVEWAL>2.0.CO;2).
- Holroyd, E. W., III, 1971: Lake-effect cloud bands as seen from weather satellites. *J. Atmos. Sci.*, **28**, 1165–1170, [https://doi.org/10.1175/1520-0469\(1971\)028<1165:LECBAS>2.0.CO;2](https://doi.org/10.1175/1520-0469(1971)028<1165:LECBAS>2.0.CO;2).
- Inoue, H. Y., and Coauthors, 2011: Finescale Doppler radar observation of a tornado and low-level misocyclones within a winter storm in the Japan Sea coastal region. *Mon. Wea. Rev.*, **139**, 351–369, <https://doi.org/10.1175/2010MWR3247.1>.
- , K. Kusunoki, K. Arai, N. Ishiyu, T. Adachi, S. Yoshida, and C. Fujiwara, 2016: Structure and evolution of misovortices observed within a convective snowband in the Japan Sea coastal-region during a cold-air outbreak on 31 December 2007. *J. Meteor. Soc. Japan*, **94**, 507–524, <https://doi.org/10.2151/jmsj.2016-029>.
- Istok, M. J., and R. J. Doviak, 1986: Analysis of the relation between Doppler spectrum width and thunderstorm turbulence. *J. Atmos. Sci.*, **43**, 2199–2214, [https://doi.org/10.1175/1520-0469\(1986\)043<2199:AOTRBD>2.0.CO;2](https://doi.org/10.1175/1520-0469(1986)043<2199:AOTRBD>2.0.CO;2).
- Khanna, S., and J. G. Brasseur, 1998: Three-dimensional buoyancy and shear-induced local structure of the atmospheric boundary layer. *J. Atmos. Sci.*, **55**, 710–743, [https://doi.org/10.1175/1520-0469\(1998\)055<0710:TDBASI>2.0.CO;2](https://doi.org/10.1175/1520-0469(1998)055<0710:TDBASI>2.0.CO;2).
- Kingsmill, D. E., 1995: Convection initiation associated with a sea-breeze front, a gust front, and their collision. *Mon. Wea. Rev.*, **123**, 2913–2933, [https://doi.org/10.1175/1520-0493\(1995\)123<2913:CIAWAS>2.0.CO;2](https://doi.org/10.1175/1520-0493(1995)123<2913:CIAWAS>2.0.CO;2).
- Kosiba, K. A., and J. Wurman, 2014: Finescale dual-Doppler analysis of hurricane boundary layer structures in Hurricane Frances (2004) at landfall. *Mon. Wea. Rev.*, **142**, 1874–1891, <https://doi.org/10.1175/MWR-D-13-00178.1>.
- , —, Y. Richardson, P. Markowski, P. Robinson, and J. Marquis, 2013: Genesis of the Goshen County, Wyoming, tornado on 5 June 2009 during VORTEX2. *Mon. Wea. Rev.*, **141**, 1157–1181, <https://doi.org/10.1175/MWR-D-12-00056.1>.
- , P. Robinson, P. W. Chan, and J. Wurman, 2014: Wind field of a nonmesocyclone anticyclonic tornado crossing the Hong Kong International Airport. *Adv. Meteor.*, **2014**, 597378, <https://doi.org/10.1155/2014/597378>.
- Kristovich, D. A. R., and R. A. Steve III, 1995: A satellite study of cloud-band frequencies over the Great Lakes. *J. Appl. Meteor.*, **34**, 2083–2090, [https://doi.org/10.1175/1520-0450\(1995\)034<2083:ASSOCB>2.0.CO;2](https://doi.org/10.1175/1520-0450(1995)034<2083:ASSOCB>2.0.CO;2).
- , and Coauthors, 2017: The Ontario Winter Lake-effect Systems (OWLLeS) field project. *Bull. Amer. Meteor. Soc.*, **98**, 315–332, <https://doi.org/10.1175/BAMS-D-15-00034.1>.
- Laird, N. F., 1999: Observation of coexisting mesoscale lake-effect vortices over the western Great Lakes. *Mon. Wea. Rev.*, **127**, 1137–1141, [https://doi.org/10.1175/1520-0493\(1999\)127<1137:OOCMLE>2.0.CO;2](https://doi.org/10.1175/1520-0493(1999)127<1137:OOCMLE>2.0.CO;2).
- , L. J. Miller, and D. A. R. Kristovich, 2001: Synthetic dual-Doppler analysis of a winter mesoscale vortex. *Mon. Wea. Rev.*, **129**, 312–331, [https://doi.org/10.1175/1520-0493\(2001\)129<0312:SDDAOA>2.0.CO;2](https://doi.org/10.1175/1520-0493(2001)129<0312:SDDAOA>2.0.CO;2).
- , N. D. Metz, L. Gaudet, C. Grasmick, L. Higgins, C. Loeser, and D. A. Zelinsky, 2017: Climatology of cold season lake-effect cloud bands for the North American Great Lakes. *Int. J. Climatol.*, **37**, 2111–2121, <https://doi.org/10.1002/joc.4838>.
- Lee, B. D., and R. B. Wilhelmson, 1997: The numerical simulation of non-supercell tornadogenesis. Part I: Initiation and evolution of pretornadic misocyclone circulation along a dry outflow boundary. *J. Atmos. Sci.*, **54**, 32–60, [https://doi.org/10.1175/1520-0469\(1997\)054<0032:TNSONS>2.0.CO;2](https://doi.org/10.1175/1520-0469(1997)054<0032:TNSONS>2.0.CO;2).
- Majcen, M., P. Markowski, Y. Richardson, D. Dowell, and J. Wurman, 2008: Multipass objective analyses of Doppler radar data. *J. Atmos. Oceanic Technol.*, **25**, 1845–1858, <https://doi.org/10.1175/2008JTECHA1089.1>.
- Markowski, P. M., and Coauthors, 2012: The pretornadic phase of the Goshen County, Wyoming, supercell of 5 June 2009 intercepted by VORTEX2. Part I: Evolution of kinematic and surface thermodynamic fields. *Mon. Wea. Rev.*, **140**, 2887–2915, <https://doi.org/10.1175/MWR-D-11-00336.1>.
- Marquis, J., Y. Richardson, and J. Wurman, 2007: Kinematic observations of misocyclones along boundaries during IHOP. *Mon. Wea. Rev.*, **135**, 1749–1768, <https://doi.org/10.1175/MWR3367.1>.
- , —, —, and P. Markowski, 2008: Single- and dual-Doppler analysis of a tornadic vortex and surrounding storm-scale flow in the Crowell, Texas, supercell of 30 April 2000. *Mon. Wea. Rev.*, **136**, 5017–5043, <https://doi.org/10.1175/2008MWR2442.1>.
- Moore, P. K., and R. E. Orville, 1990: Lightning characteristics in lake-effect thunderstorms. *Mon. Wea. Rev.*, **118**, 1767–1782, [https://doi.org/10.1175/1520-0493\(1990\)118<1767:LCILET>2.0.CO;2](https://doi.org/10.1175/1520-0493(1990)118<1767:LCILET>2.0.CO;2).
- Mulholland, J. P., J. Frame, S. Nesbitt, S. Steiger, K. Kosiba, and J. Wurman, 2017: Observations of misovortices within a long-lake-axis-parallel lake-effect snowband during the OWLeS project. *Mon. Wea. Rev.*, **145**, 3265–3291, <https://doi.org/10.1175/MWR-D-16-0430.1>.
- National Weather Service, 2014: Lake effect summary: November 17–19, 2014. National Weather Service (NWS) Buffalo, NY, accessed 3 December 2019, https://www.weather.gov/buf/lake1415_stormb.html.

- Niziol, T. A., 1987: Operational forecasting of lake effect snowfall in western and central New York. *Wea. Forecasting*, **2**, 310–321, [https://doi.org/10.1175/1520-0434\(1987\)002<0310:OFOLES>2.0.CO;2](https://doi.org/10.1175/1520-0434(1987)002<0310:OFOLES>2.0.CO;2).
- , W. R. Snyder, and J. S. Waldstreicher, 1995: Winter weather forecasting throughout the eastern United States. Part IV: Lake effect snow. *Wea. Forecasting*, **10**, 61–77, [https://doi.org/10.1175/1520-0434\(1995\)010<0061:WWFTTE>2.0.CO;2](https://doi.org/10.1175/1520-0434(1995)010<0061:WWFTTE>2.0.CO;2).
- Pease, S. R., W. A. Lyons, C. S. Keen, and M. Hjelmfelt, 1988: Mesoscale spiral vortex embedded within a Lake Michigan snow squall band: High resolution satellite observations and numerical model simulations. *Mon. Wea. Rev.*, **116**, 1374–1380, [https://doi.org/10.1175/1520-0493\(1988\)116<1374:MSVEWA>2.0.CO;2](https://doi.org/10.1175/1520-0493(1988)116<1374:MSVEWA>2.0.CO;2).
- Pietrycha, A. E., and E. N. Rasmussen, 2004: Finescale surface observations of the dryline: A mobile mesonet perspective. *Wea. Forecasting*, **19**, 1075–1088, <https://doi.org/10.1175/819.1>.
- Rodriguez, Y., D. A. Kristovich, and M. R. Hjelmfelt, 2007: Lake-to-lake cloud bands: Frequencies and locations. *Mon. Wea. Rev.*, **135**, 4202–4213, <https://doi.org/10.1175/2007MWR1960.1>.
- Steiger, S. M., and Coauthors, 2013: Circulations, bounded weak echo regions, and horizontal vortices observed within long lake-axis-parallel lake-effect storms by the Doppler on Wheels. *Mon. Wea. Rev.*, **141**, 2821–2840, <https://doi.org/10.1175/MWR-D-12-00226.1>.
- , T. Kranz, and T. Letcher, 2018: Thunderstorm characteristics during the Ontario Winter Lake-effect Systems project. *J. Appl. Meteor. Climatol.*, **57**, 853–874, <https://doi.org/10.1175/JAMC-D-17-0188.1>.
- Trapp, R. J., and C. A. Doswell, 2000: Radar data objective analysis. *J. Atmos. Oceanic Technol.*, **17**, 105–120, [https://doi.org/10.1175/1520-0426\(2000\)017<0105:RDOA>2.0.CO;2](https://doi.org/10.1175/1520-0426(2000)017<0105:RDOA>2.0.CO;2).
- Vivekanandan, J., D. S. Zrnić, S. Ellis, D. Oye, A. V. Ryzhkov, and J. M. Straka, 1999: Cloud microphysics retrieval using S-band dual-polarization radar measurements. *Bull. Amer. Meteor. Soc.*, **80**, 381–388, [https://doi.org/10.1175/1520-0477\(1999\)080<0381:CMRUSB>2.0.CO;2](https://doi.org/10.1175/1520-0477(1999)080<0381:CMRUSB>2.0.CO;2).
- Wakimoto, R. M., and J. W. Wilson, 1989: Non-supercell tornadoes. *Mon. Wea. Rev.*, **117**, 1113–1140, [https://doi.org/10.1175/1520-0493\(1989\)117<1113:NST>2.0.CO;2](https://doi.org/10.1175/1520-0493(1989)117<1113:NST>2.0.CO;2).
- Winstead, N. S., R. M. Schaaf, and P. D. Mourad, 2001: Synthetic Aperture Radar observations of the surface signatures of cold-season bands over the Great Lakes. *Wea. Forecasting*, **16**, 315–328, [https://doi.org/10.1175/1520-0434\(2001\)016<0315:SAROOT>2.0.CO;2](https://doi.org/10.1175/1520-0434(2001)016<0315:SAROOT>2.0.CO;2).
- Wurman, J., 2001: The DOW mobile multiple Doppler network. Preprints, *30th Int. Conf. on Radar Meteorology*, Munich, Germany, Amer. Meteor. Soc., 95–97.
- , and K. Kosiba, 2013: Finescale radar observations of tornado and mesocyclone structures. *Wea. Forecasting*, **28**, 1157–1174, <https://doi.org/10.1175/WAF-D-12-00127.1>.
- , and —, 2018: The role of small-scale vortices in enhancing surface winds and damage in Hurricane Harvey (2017). *Mon. Wea. Rev.*, **146**, 713–722, <https://doi.org/10.1175/MWR-D-17-0327.1>.
- , J. Straka, and E. Rasmussen, 1996: Fine scale Doppler observation of tornadoes. *Science*, **272**, 1774–1777, <https://doi.org/10.1126/science.272.5269.1774>.
- , Y. Richardson, C. Alexander, S. Weygandt, and P. F. Zhang, 2007: Dual-Doppler analysis of winds and vorticity budget terms near a tornado. *Mon. Wea. Rev.*, **135**, 2392–2405, <https://doi.org/10.1175/MWR3404.1>.
- , K. Kosiba, P. Markowski, Y. Richardson, D. Dowell, and P. Robinson, 2010: Finescale single- and dual-Doppler analysis of tornado intensification, maintenance, and dissipation in the Orleans, Nebraska, supercell. *Mon. Wea. Rev.*, **138**, 4439–4455, <https://doi.org/10.1175/2010MWR3330.1>.